nature communications

Article

https://doi.org/10.1038/s41467-025-67698-1

Antibody-conjugated mesenchymal stromal cell drug delivery system for the treatment of autoimmune diseases in mice

Received: 1 May 2025

Accepted: 5 December 2025

Published online: 22 January 2026

Check for updates

Qian Xie[1,8] ✉, Yanni Shen[1,8], Jianhui Liang[1], Chang Fu[1], Xiangfu Du[2], Shuya Huang[1,3], Bing Song[4,5,6], Lei Chen[3,7] ✉ & Yan Wang[1] ✉

Autoimmune diseases (AIDs), such as psoriasis and rheumatoid arthritis, are driven by immune dysfunction, leading to chronic inflammation and tissue damage. Mesenchymal stromal cells (MSCs) possess immunomodulatory and tissue repair properties; however, the therapeutic applicability of MSCs faces limitations due to the low homing efficiency upon systemic infusion. Inspired by antibody-drug conjugates (ADC), here we develop an antibody-conjugated MSC-based drug delivery system (AcM-DDS) that combines CD4 monoclonal antibody-conjugated MSC (CD4-mBMSC) with liposome-encapsulated Cedirogant, a RORγt inverse agonist. AcM-DDS targets $CD4^+$ T cells, key drivers of AID, and precisely delivers RORγt antagonists to suppress Th17-mediated inflammation. In mouse models of imiquimod-induced psoriasis and collagen-induced arthritis, AcM-DDS enhances MSC homing to inflamed tissues, reduces Th17 activity, lowers pro-inflammatory cytokine production, and preserves cartilage and bone integrity. Thus, our results indicate the promising applicability of our engineered platform for targeted immune modulation and provide support for the suitability of this therapeutic approach for the treatment of AIDs.

Mesenchymal stromal cells (MSC) have shown promising potential in the treatment of autoimmune diseases (AID) such as psoriasis (PO)[1–3], systemic lupus erythematosus (SLE)[4–6], multiple sclerosis (MS)[7], inflammatory bowel disease (IBD)[8–10], and rheumatoid arthritis (RA)[11–13]. Their ability to modulate immune responses and promote tissue repair makes them a valuable therapeutic option for these conditions. MSCs exert therapeutic effects through multiple mechanisms: secreting anti-inflammatory factors and exosomes that suppress aberrant T and B cell activation[14,15], promoting the expansion of regulatory T cells (Treg) to restore immune homeostasis[16], and migrating to damaged tissues to facilitate tissue regeneration[17,18]. A key advantage of MSC is their availability from multiple sources, such as bone marrow, adipose tissue, and umbilical cords[19]. Their low expression of major histocompatibility complex molecules reduces the risk of immune rejection in allogeneic transplantation[20], and their genetic stability and multipotency during in vitro expansion further enhance their clinical utility[21,22]. Clinical studies have demonstrated that MSC transplantation effectively reduces psoriatic lesions and alleviates pruritus[1–3], while also showing safety and efficacy in treating RA[11–13], SLE[4–6], MS[7], and IBD[8–10]. These findings highlight the immense therapeutic potential and clinical value of MSCs in managing AIDs.

[1]Center for Translational Medicine Research and Development, Shenzhen Institutes of Advanced Technology, Chinese Academy of Sciences, Shenzhen, China. [2]Fujian Provincial Key Laboratory of Innovative Drug Target Research, School of Pharmaceutical Sciences, Xiamen University, Xiamen, China. [3]School of Life Science and Technology, Key Laboratory of Developmental Genes and Human Disease, Southeast University, Nanjing, China. [4]Faculty of Biomedical Engineering, Shenzhen University of Advanced Technology, Shenzhen, China. [5]State Key Laboratory of Biomedical Imaging Science and System, Shenzhen, China. [6]School of Dentistry, Cardiff University, Cardiff, UK. [7]Institute of Microphysiological Systems, Southeast University, Nanjing, China. [8]These authors contributed equally: Qian Xie, Yanni Shen. ✉e-mail: qian.xie2@siat.ac.cn; leichen@seu.edu.cn; yan.wang@siat.ac.cn

However, the low homing efficiency of MSCs remains a critical limitation in their clinical application for AID[23]. Following systemic administration, a large proportion of MSCs become trapped in non-target organs, failing to migrate effectively to sites of inflammation or tissue damage, thereby reducing therapeutic efficacy[24]. MSC homing is mediated by chemokine gradients, adhesion molecules, and their corresponding receptors, which guide MSCs to inflamed or damaged tissues[25]. However, under pathological conditions, the dysregulated expression of chemokines and adhesion molecules, along with a hostile inflammatory microenvironment, often impairs these mechanisms, leading to inefficient MSC migration and retention at target sites[26]. Consequently, higher doses of MSCs are required to achieve the desired therapeutic effects, which not only increases treatment costs but also raises the risk of adverse effects[27]. To enhance the homing efficiency of BMSCs, genetically modified BMSCs overexpressing receptors such as CXCR6 and CCR2 have been developed, enabling improved targeting to inflamed sites via increased responsiveness to inflammatory signals[28,29]. However, the limitations of genetic modification, including safety concerns, hinder their widespread application[30]. Therefore, enhancing MSC homing efficiency is essential to improving their clinical efficacy and expanding their therapeutic applications in AIDs (Fig. 1a).

Antibody-drug conjugates (ADC), which combine monoclonal antibodies (Ab) with cytotoxic agents[31], offer a potential solution. By exploiting antibody specificity, ADCs ensure precise drug localization at pathological sites, minimizing off-target effects, and maximizing therapeutic efficacy[32]. Inspired by this concept, Antibody-conjugated MSCs (Ac-MSC) have been developed to improve MSC homing (Fig. 1b). Conjugating MSCs with disease-specific antibodies enables these cells to selectively target inflamed or damaged tissues by binding to overexpressed pathological markers. This approach enhances MSC accumulation at disease sites, amplifying their immunomodulatory and regenerative potential.

Additionally, Ac-MSCs can function as “live cell drug carriers”, internalizing therapeutic agents and releasing them within the inflammatory microenvironment. Unlike ADCs, which require target antigens (Ag) to undergo receptor-mediated endocytosis for efficient payload delivery[33], Ac-MSCs transport their internalized payload to inflammation sites, where it is extracellularly released and diffuses into adjacent target cells (Fig. 1b). This mechanism eliminates the need for antigen internalization, allowing Ac-MSCs to target a wide range of surface proteins and achieve site-specific drug accumulation rather than cell-restricted delivery. By integrating targeted drug delivery with the inherent therapeutic functions of MSCs, this strategy reduces required cell doses, lowering costs and minimizing systemic side effects. By combining ADC targeting precision with MSC multifunctionality, the Antibody-conjugated MSC Drug Delivery System (AcM-DDS) represents a promising strategy to enhance the efficacy of MSC-based therapies and expand their clinical applications in AID.

Lesion sites in AIDs are characterized by an accumulation of aberrantly activated $CD4^+$ T cells, which drive immune dysregulation and inflammation[34]. Among $CD4^+$ T cells, Th17 cells play a pivotal role in autoimmune pathogenesis by secreting pro-inflammatory cytokines such as IL-17A[35–37]. However, BMSCs do not significantly inhibit Th17 cells in some AID patients, which partly explains their uncertain clinical efficacy[38]. The differentiation and function of Th17 cells are regulated by the transcription factor RAR-related orphan receptor gamma t (RORγt), whose hyperactivation in AID drives excessive IL-17A production, exacerbating inflammation and disrupting immune homeostasis[39,40]. Although targeting RORγt with inverse agonists such as Cedirogant (ABBV-157) stabilizes the protein in its inactive conformation and represents a promising therapeutic approach for modulating Th17 activity[41], the clinical development of these compounds has been hindered by off-target toxicities[42].

To overcome these limitations, we conjugated CD4 monoclonal antibodies (CD4mAb) to mouse bone marrow-derived MSC (mBMSC) using bioorthogonal chemistry, generating CD4mAb-BMSCs that selectively targeted $CD4^+$ T cells and localized to lesion sites (Fig. 1c). We proposed that augmenting BMSCs with a small-molecule drug capable of directly suppressing Th17 cells would improve their therapeutic efficacy against AIDs. Accordingly, CD4mAb-BMSCs were loaded with liposomes encapsulating Cedirogant, leveraging the high encapsulation efficiency and biocompatibility of liposomes for controlled delivery. This AcM-DDS framework therefore integrates targeted recognition of pathogenic T cells with localized pharmacologic inhibition of RORγt, establishing a coherent strategy for restoring immune balance in AID.

Here we present the application of this AcM-DDS platform for the treatment of AIDs. The system effectively suppresses Th17 differentiation and IL-17A overexpression in two Th17-driven disease models: the imiquimod (IMQ)-induced PO model and the collagen-induced arthritis (CIA) model. In PO mice, AcM-DDS significantly inhibits Th17 differentiation and IL-17A overexpression, reduces pro-inflammatory cytokine release, alleviates inflammation and improves skin lesions (Fig. 1d). In CIA mice, it downregulates joint Th17 activity and IL-17A levels, thereby mitigating cartilage and bone destruction (Fig. 1e). These results demonstrate the therapeutic potential of AcM-DDS in controlling Th17-mediated pathology and highlight its broader applicability to other inflammatory disorders characterized by dysregulated T-cell responses.

Results

Enhanced homing efficiency of CD4 antibody-conjugated mBMSC to inflammatory lesions in PO Mice

Bioorthogonal technology enables cell membrane modification while preserving biological integrity[43]. Ac_4ManNAz metabolically labels cells by introducing azide groups into membrane glycoproteins and glycolipids via the sialic acid biosynthesis pathway[44]. Simultaneously, lysine residues on antibodies react with DBCO-NHS esters to yield DBCO-modified antibodies[43], which rapidly conjugate with azide-functionalized MSC membranes through catalyst-free click chemistry at room temperature, generating antibody-conjugated MSC (Fig. 2a).

Th17 cells are central to the pathogenesis of psoriasiform inflammation. Consistent with this, histological analysis revealed that most $CD4^+$ T cells in psoriasiform lesions are Th17 cells (Supplementary Fig. 1). Additionally, the CD4 antibody Ibalizumab has been approved by the FDA, indicating a favorable safety profile[45]. More importantly, CD4 here is not a therapeutic target but serves to direct BMSC toward inflamed regions. Based on this evidence, CD4mAb were conjugated onto metabolically azidated mBMSC to generate CD4-mBMSC with selective affinity for $CD4^+$ T cells. Confocal microscopy confirmed successful azide incorporation on the mBMSC membrane after Ac_4ManNAz treatment, as evidenced by robust DBCO-FAM (a green fluorescent dye) fluorescence (Fig. 2b). Subsequently, CD4mAb were conjugated with DBCO-PEG_4-NHS ester through amide coupling and purified by ultrafiltration, and then co-incubated with N_3-mBMSC via bioorthogonal click chemistry to obtain CD4-mBMSC. Flow cytometry analysis revealed a concentration-dependent increase in fluorescence intensity upon incubation of N_3-mBMSC with DBCO-CD4mAb-FITC. Quantitative fluorescence analysis indicated that when 25 μg of DBCO-CD4mAb-FITC was conjugated with 1×10^6 N_3-mBMSC, approximately 2500 antibody molecules anchored per cell on average (Fig. 2c). Confocal microscopy further confirmed successful surface conjugation of CD4mAb (Fig. 2d).

To validate the binding capability of CD4-mBMSC, $CD4^+$ T cells were isolated from the spleens of C57BL/6 J mice using magnetic bead sorting (Supplementary Fig. 2a). N_3-mBMSC and CD4-mBMSC pre-labeled with Dil (a red fluorescent membrane dye) and co-cultured with $CD4^+$ T cells. Confocal imaging revealed that, compared to N_3-mBMSC, CD4-mBMSC exhibited significantly

https://doi.org/10.1038/s41467-025-67698-1

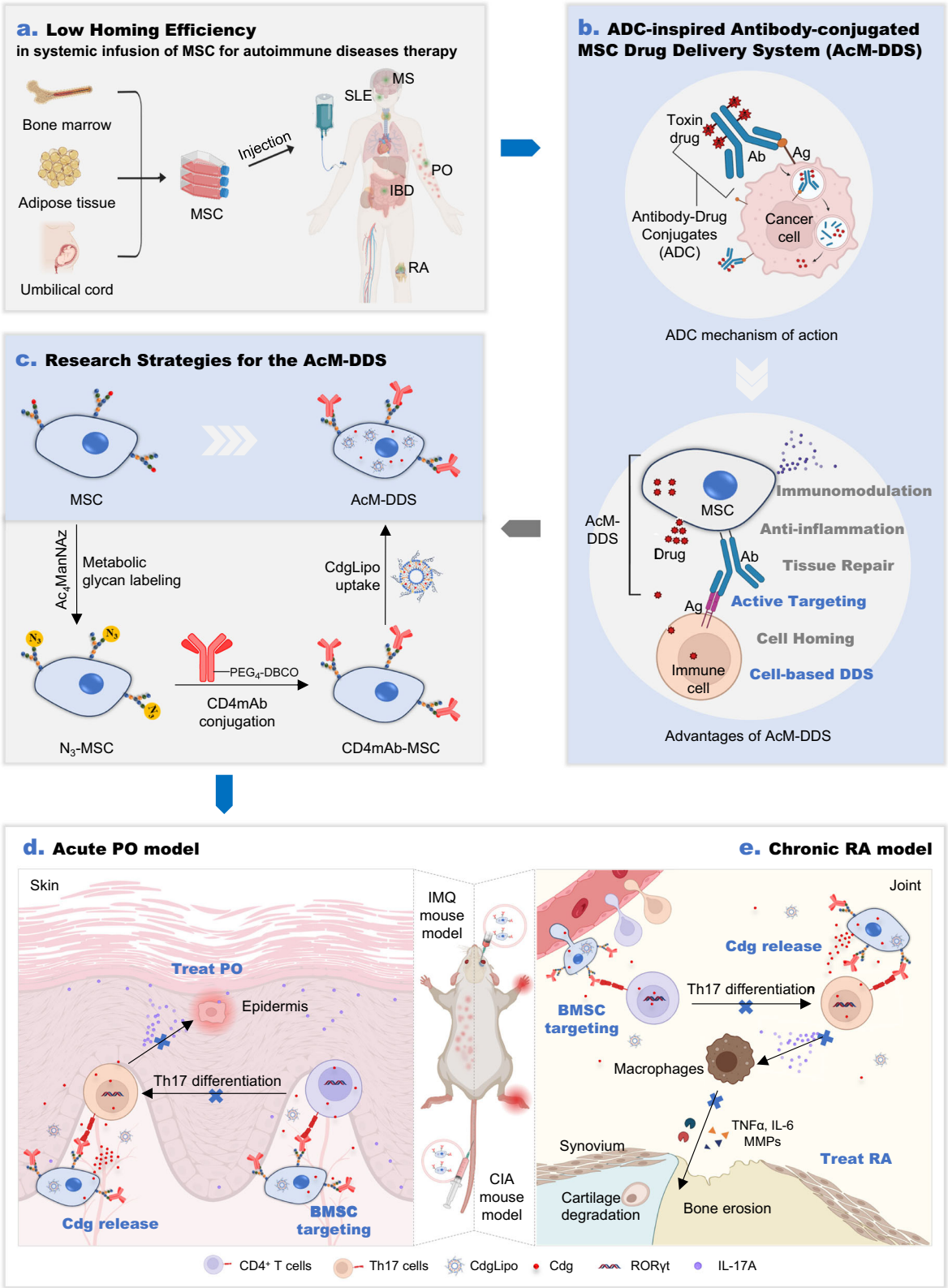

Fig. 1 | Concept, construction and therapeutic application of the AcM-DDS. **a** Limited homing and efficacy of systemically infused MSC. **b** Design of antibody-conjugated MSC for antigen-specific targeting and local drug release. **c** Construction of AcM-DDS by metabolic glycan labeling and antibody conjugation, combined with intracellular drug loading. As an application example, CD4mAb-conjugated BMSC loaded with RORγt inverse agonists demonstrate therapeutic efficacy in the IMQ-induced PO model (**d**) and the CIA model (**e**). Created in BioRender. Li, J. (2026) https://BioRender.com/rmjk4bf.

https://doi.org/10.1038/s41467-025-67698-1

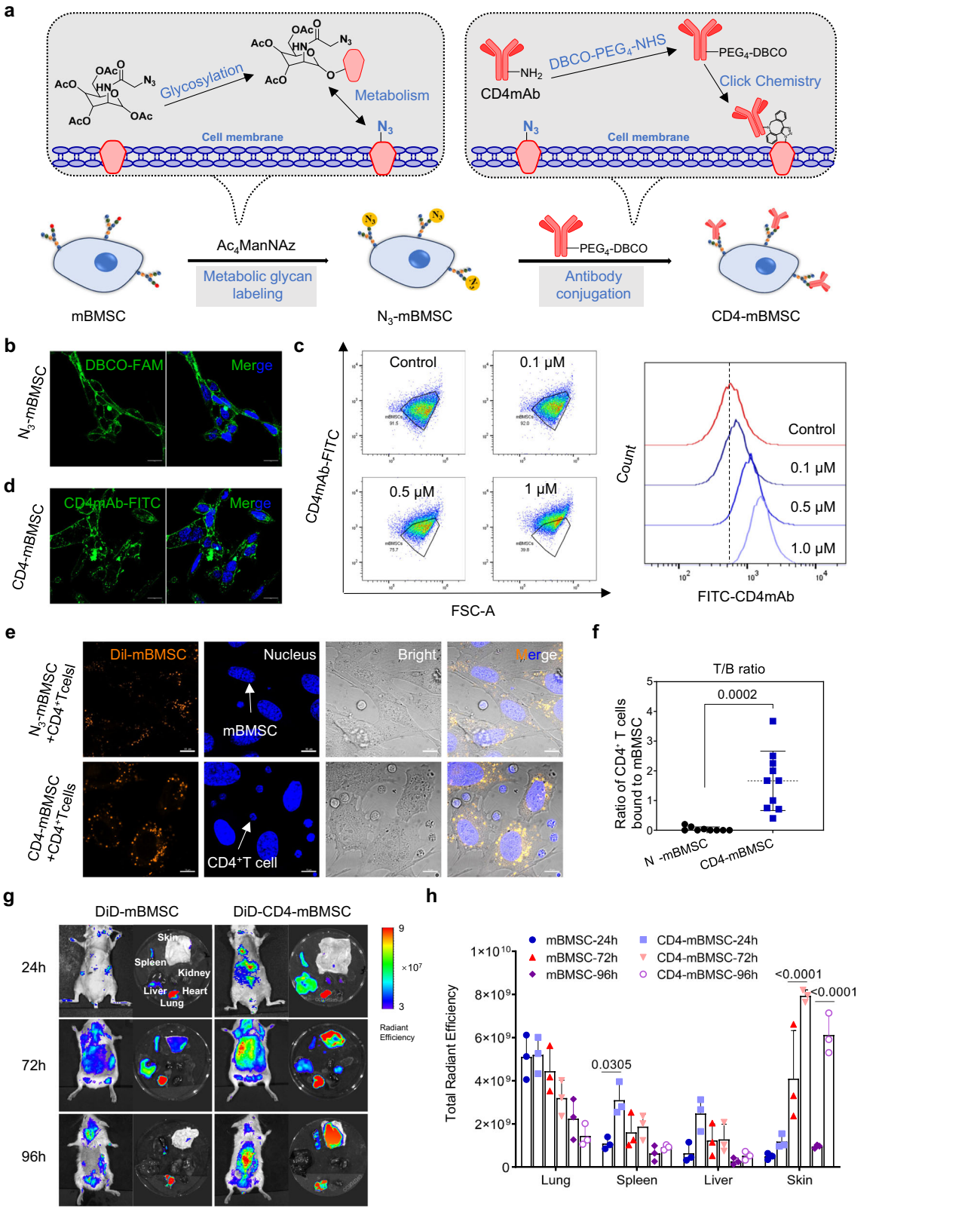

enhanced binding to multiple CD4⁺ T cells, confirming their targeted binding capacity toward CD4⁺ T cells in vitro (Fig. 2e, f, Supplementary Fig. 2b, c). Furthermore, the in vivo targeting efficiency of CD4-mBMSC was evaluated in IMQ-induced PO mice. DiD (a near-infrared lipophilic fluorescent dye)-labeled mBMSC and CD4-mBMSC were intravenously administered, followed by in vivo imaging using IVIS. CD4-mBMSC showed faster accumulation and longer retention in the spleen and inflamed dorsal skin regions than unmodified mBMSC, indicating superior in vivo targeting efficiency (Fig. 2g, h). Consistently, flow cytometric analysis of dorsal skin tissues 72 h post-injection revealed a significantly higher proportion of DiD⁺ cells in the CD4-mBMSC group, further confirming enhanced accumulation of CD4-modified mBMSC in inflamed skin (Supplementary Fig. 2d).

Fig. 2 | Construction and targeting validation of CD4mAb-conjugated mBMSC. **a** Schematic illustration of the strategy for constructing CD4-mBMSC. **b** Confocal fluorescence images of mBMSC metabolically labeled with $Ac_4ManNAz$ and reacted with DBCO-FAM (100 nM). Scale bars, 20 μm ($n = 3$ independent experiments). **c** Flow cytometry analysis of fluorescence intensity in N_3-mBMSC incubated with increasing concentrations of DBCO-CD4mAb-FITC (no gating applied; all cells included). **d** Confocal fluorescence images of N_3-mBMSC reacting with DBCO-CD4mAb-FITC fluorescent antibody (100 nM). Scale bars, 20 μm (n = 3 independent experiments). **e** Confocal fluorescence imaging of Dil-stained N_3-mBMSC or CD4-mBMSC (orange) co-cultured with $CD4^+$ T cells for 6 h. Scale bars, 10 μm ($n = 3$ independent experiments). **f** Quantification of the ratio of $CD4^+$ T cells bound to mBMSC per field. $n = 10$ randomly selected fields from three independent experiments. **g** In vivo fluorescence imaging acquired using an IVIS imaging system of DiD-stained mBMSC or CD4-mBMSC in IMQ-induced PO mice at 24 h, 72 h, and 96 h post intravenous injection. **h**, Quantification of fluorescence distribution in lungs, spleen, liver, and skin. $n = 3$ mice per group. Data are presented as means ± SD, and are analyzed by unpaired two-tailed t test (**f**) or two-way ANOVA followed by Tukey's multiple comparisons test (**h**). Source data are provided as a Source Data file.

CD4-mBMSC uptake Cedirogant-loaded liposome (CdgLipo) to construct AcM-DDS

RORγt inverse agonists suppress IL-17A for AID treatment; however, challenges related to selectivity and off-target effects have raised safety concerns, resulting in the discontinuation of clinical trials[46]. To overcome these limitations, we aimed to load RORγt inverse agonists into CD4-mBMSC to enable targeted drug delivery at the disease site. For this purpose, we encapsulated Cedirogant (Cdg)—a Phase II RORγt inverse agonist previously discontinued due to safety issues[47]—into liposomes (CdgLipo) composed of DPPC, DSPE-PEG2000, and cholesterol (Fig. 3a). HPLC analysis revealed that the liposomes had a drug loading capacity of approximately 8.48% (w/w, drug-to-lipid ratio) and an encapsulation efficiency of 92.8% (percentage of total Cdg encapsulated in liposomes). Characterization of CdgLipo, using transmission electron microscopy (TEM) (Supplementary Fig. 3a), Malvern particle size analysis (Supplementary Fig. 3b) and nano-flow cytometry (Supplementary Fig. 3c), revealed an average particle size of 76.3 ± 14.8 nm, with a particle concentration of 9.55×10^{10} particles/mL (Supplementary Fig. 3d). No significant changes in particle size were observed over 7 days, but a marked increase in size was noted over a longer period (Supplementary Fig. 3e). The zeta potential remained stable, with no significant fluctuations over 27 days (Supplementary Fig. 3f). After 12 hours of incubation with mBMSC, Calcein-AM/PI staining showed no signs of cytotoxicity (Supplementary Fig. 3g).

Then, CD4-mBMSC were incubated with CdgLipo for one hour, and intracellular localization of liposomes was observed predominantly around mitochondria by Bio-TEM (Fig. 3b). To further investigate cellular uptake, Cy5-labeled CdgLipo (Cy5-CdgLipo) was compared to free Cy5, showing superior internalization by mBMSC (Supplementary movies 1 and 2). Mitochondrial and lysosomal staining showed a strong colocalization of Cy5-CdgLipo fluorescence with mitochondria, indicating effective lysosomal escape (Fig. 3c). Furthermore, quantitative fluorescence analysis based on Cy5 intensity allowed estimation of nanoparticle uptake per cell, indicating that each CD4-mBMSC internalized approximately 1.15×10^4 CdgLipo particles on average.

To evaluate drug release kinetics, we assessed Cdg release from CdgLipo alone and from CD4-mBMSC after internalization. While free CdgLipo exhibited nearly complete Cdg release within 48 hours, intracellular CdgLipo displayed a more controlled release profile, with approximately 76.31% of Cdg released over the same period (Fig. 3d). Interestingly, in a separate experiment, we observed that both N_3-mBMSC and mBMSC internalized Cy5Lipo with comparable efficiency (Fig. 3e). But N_3-mBMSC released Cy5 significantly more slowly (Fig. 3f, Supplementary Fig. 4a). This suggests that glycoprotein azidation on the cell membrane may impact small molecule efflux. Further investigation using the P-glycoprotein inhibitor verapamil revealed that N_3-mBMSC demonstrated an efflux capacity comparable to verapamil-treated mBMSC (Supplementary Fig. 4b). These findings indicate that azidation impairs P-glycoprotein-mediated efflux in mBMSC, enhancing their potential for drug delivery applications.

Furthermore, we analyzed osteogenic differentiation in four cell groups: mBMSC, mBMSC incubated with CdgLipo, CD4-mBMSC, and AcM-DDS. ALP staining (early osteogenesis) and Alizarin Red (AR) staining (late osteogenesis) showed no significant differences in differentiation capacity among these groups (Fig. 3g). Chondrogenic differentiation, assessed by Alcian blue (AB) staining of cell-derived spheroids (Fig. 3h) and adipogenic differentiation, evaluated by Oil Red O (ORO) staining (Fig. 3i), also revealed no appreciable differences, indicating comparable chondrogenic and adipogenic potentials.

In addition, we further performed bulk RNA-Seq analysis and found that both antibody-conjugated BMSC and antibody-conjugated, drug-loaded BMSC affect less than 0.2% of the total transcriptome ($\log_2FC > 2$ or < -2, $p < 0.05$). Moreover, the highly variable genes were not involved in signaling pathways related to adipogenic, osteogenic, or chondrogenic differentiation of BMSC (Supplementary Fig. 5a-e). Notably, the expression levels of Fgf2 and Ptgs2—both known to promote BMSC proliferation[48,49]—were markedly increased, which is consistent with our observation that AcM-DDS exhibited enhanced proliferation compared to mBMSC (Supplementary Figs. 5f, 3j). Meanwhile, live/dead staining showed no notable differences in viability among the groups (Fig. 3k). All of these results suggest that the AcM-DDS system, constructed using CdgLipo and CD4-mBMSC, preserves MSC stemness and proliferation capacity while demonstrating superior drug delivery potential.

AcM-DDS effectively treats IMQ-induced PO in an acute inflammation mouse model

The IMQ-induced PO model is an acute inflammatory mouse model induced by topical IMQ, closely mimicking the pathological and immune features of human PO, and widely utilized in the preclinical development of PO therapies[50]. In this study, dorsal hair was removed from male Balb/c mice, followed by topical Vaseline or IMQ application. IMQ-treated mice were randomly assigned to five groups: Model, mBMSC, CD4-mBMSC, CdgLipo, and AcM-DDS. For MSC-based treatments, 1×10^6 cells per mouse were administered via tail vein injection, which is a commonly used dosage and route in preclinical MSC therapy studies for autoimmune diseases[51], ensuring reliable efficacy and safety. For Cdg, the administered dose (4.5 mg/kg) corresponded to the maximal amount of drug internalized by 1×10^6 mBMSC. IMQ and Vaseline were applied daily for five days, and all mice were sacrificed on day 7 for analysis (Fig. 4a).

Following IMQ application, all IMQ-treated groups exhibit a slight reduction in body weight compared to the Sham group (Supplementary Fig. 6a). Dorsal skin lesions developed by day 4, with scaling appearing on day 5 in all groups except AcM-DDS (Supplementary Fig. 6b). By day 7, the AcM-DDS group remained largely free of scaling, while the mBMSC, CD4-mBMSC, and CdgLipo groups showed marked improvement over the Model group. Notably, CD4-mBMSC group exhibited superior therapeutic effects compared to mBMSC, indicating that antibody conjugation enhances MSC-based therapy (Fig. 4b). Histological analysis supported these findings. The hematoxylin and eosin (H&E) staining revealed severe epidermal thickening and pronounced wrinkling in the Model group, which were significantly alleviated in all treatment groups, with the most pronounced improvement in AcM-DDS (Fig. 4c, d). Additionally, Masson staining demonstrated that AcM-DDS markedly reduced fiber deposition in the dorsal skin (Fig. 4e, f).

For comparison, additional groups were treated with the positive control methotrexate[52] (MTX, daily oral gavage), free Cdg (single

https://doi.org/10.1038/s41467-025-67698-1

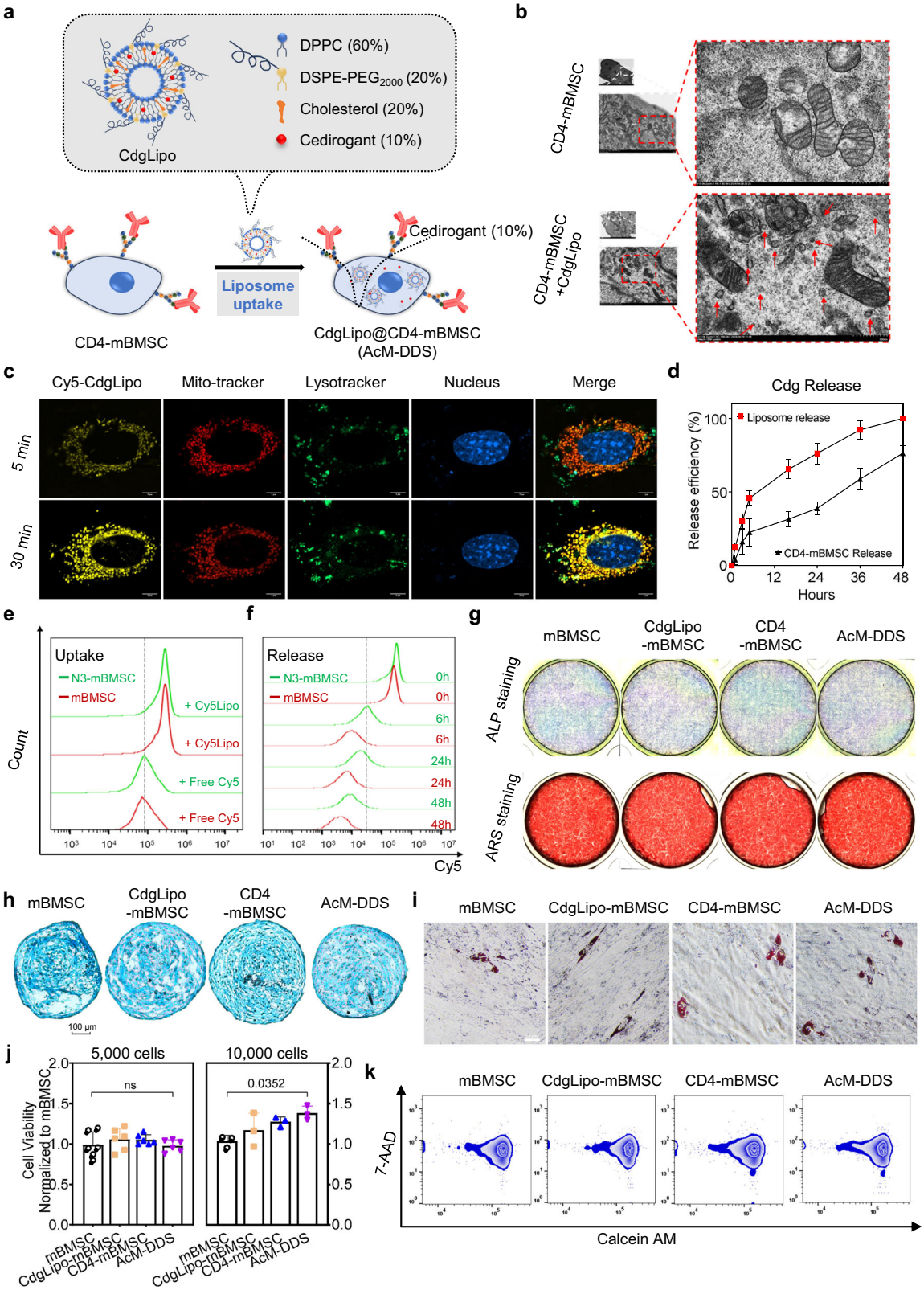

intravenous injection), or repeated doses of CdgLipo (two intravenous injections during the 5-day IMQ treatment period). Based on the daily assessment of skin scaling, along with H&E and Masson staining results, both MTX and free Cdg induced moderate improvements, while repeated CdgLipo dosing produced slightly better outcomes. However, none of these treatments achieved the therapeutic efficacy of AcM-DDS, as evidenced by more limited lesion resolution and histopathological recovery. Consistently, the AcM-DDS group exhibited the most pronounced reductions in spleen enlargement, epidermal thickness, and dermal fibrosis (Supplementary Fig. 7a–i).

To investigate whether ACM-DDS regulates Th17-cell-mediated inflammation, immunofluorescence (IF) staining for CD4, IL-17A, and RORγt was performed on frozen skin sections. IL-17A and RORγt were highly expressed at the epidermal-dermal junction in the Model group

Fig. 3 | Internalization of CdgLipo by CD4-mBMSC for AcM-DDS construction and functional characterization. a Composition and formulation details of CdgLipo, along with a schematic representation illustrating its uptake by CD4-mBMSC for AcM-DDS construction. **b** Bio-TEM images confirming the intracellular localization of CdgLipo within CD4-mBMSC, with arrows indicating internalized liposome. Scale bar, 500 nm (n = 3 samples per group). **c** Confocal microscopy visualization of fluorescently labeled Cy5-loaded CdgLipo uptake by CD4-mBMSC, verifying successful internalization. Scale bar, 5 μm (n = 3 independent experiments). **d** Cdg release kinetics from CdgLipo and CD4-mBMSC following CdgLipo uptake (n = 3 independent experiments). **e** Comparative analysis of Cy5-labeled CdgLipo versus free Cy5 uptake efficiency in mBMSC and N_3-mBMSC over the same incubation period. n = 2 independent experiments. **f** Quantification of Cy5 release from mBMSC and N_3-mBMSC one-hour post-internalization of Cy5-CdgLipo, evaluating retention and controlled release characteristics. n = 3 independent experiments. **g** Osteogenic differentiation potential of four experimental groups (mBMSC, CdgLipo-mBMSC, CD4-mBMSC, and AcM-DDS) assessed through early-stage ALP staining and late-stage AR staining. AB staining results for chondrogenic differentiation (**h**) and ORO staining results for adipogenic differentiation (**i**) in the four cell groups mentioned above. $n = 3$ independent experiments (**g**–**i**). Scale bar, 50 μm (**i**). **j** Cell proliferation capacity of the four groups evaluated via CCK-8 assay. For cultures seeded at 10,000 cells per well, $n = 6$ samples per group, while for cultures seeded at 5000 cells per well, $n = 3$ samples per group. **k** Live/dead cell analysis of the four groups using Calcein-AM/7-AAD staining to assess cytotoxicity (no gating applied; all cells included). $n = 2$ independent experiments. Data are presented as means ± SD (**d**, **j**), and are analyzed by one-way ANOVA followed by Tukey's multiple comparisons test (**j**). ns = no significance. Source data are provided as Source Data file.

but significantly reduced in the mBMSC and CdgLipo groups, slightly higher in CD4-mBMSC, and nearly absent in AcM-DDS (Fig. 4g–i). CD4 expression was moderately reduced in all treatment groups compared with the Model group, with no significant differences among them (Supplementary Fig. 8). Collectively, these results demonstrate that AcM-DDS achieves superior therapeutic efficacy primarily through potent inhibition of Th17-cell-mediated inflammation in the skin.

AcM-DDS attenuates Th17-driven cytokine expression and systemic inflammation in IMQ-induced PO mice

To further elucidate the immunomodulatory effects of AcM-DDS, we first evaluate local cytokine expression in the dorsal skin of IMQ-induced PO mice. IF staining revealed marked upregulation of IL-21 and IL-22 in the Model group, both of which are critical downstream mediators of Th17-driven inflammation. In contrast, AcM-DDS treatment led to a pronounced suppression of IL-21 and IL-22 expression compared with other treatment groups (Fig. 5a–d), suggesting potent inhibition of Th17-associated inflammatory pathways.

Luminex multiplex assay was performed to assess the expression of 22 inflammatory cytokines in total protein extracts from dorsal skin tissues (Fig. 5e). Compared to the Sham group, the Model group exhibited a significantly elevation in multiple pro-inflammatory cytokines, including Eotaxin, G-CSF, GM-CSF, IL-12p40, IL-12p70, IL-17A, IL-1α, IL-1β, IL-4, KC, MIP-1α, and MIP-1β (Supplementary Fig. 9). Treatment with AcM-DDS, as well as mBMSC, CD4-mBMSC, and CdgLipo, led to an overall downward trend in these cytokines, indicating effective attenuation of inflammation. Notably, although reductions in IL-17A and GM-CSF were comparable among the cell-based and liposomal treatments (Fig. 5f, g), IF analysis revealed a more pronounced local suppression of IL-17A, IL-21 and IL-22 by AcM-DDS, suggesting that its superior modulation may primarily occur at the tissue microenvironment level rather than in total tissue cytokine content. Interestingly, CD4-mBMSC showed stronger suppression of G-CSF and IL-12p40 than mBMSC, suggesting that even in the absence of Cdg loading, enhanced localization and prolonged residence of MSC at inflamed sites contribute significantly to their anti-inflammatory activity. Although IL-17A and RORγt expression appeared only partially reduced in the CD4-mBMSC group by IF, this likely reflects localized measurement limits, as the Luminex assay—analyzing whole-skin lysates from multiple cellular sources—revealed a pronounced overall suppression of inflammatory cytokines.

Given that systemic inflammation in the IMQ-induced PO model often manifests as splenomegaly and elevated IL-17A levels[50], we next examined the spleen to assess potential systemic effects of AcM-DDS. Consistent with prior observations, significant splenic enlargement was observed in all IMQ-treated groups compared to Sham (Supplementary Fig. 10). Histological examination revealed substantial red pulp expansion and tissue edema in the Model group, which persisted in the mBMSC, CD4-mBMSC, and CdgLipo groups but was substantially alleviated by AcM-DDS treatment (Fig. 5h-i). Additionally, H&E staining of heart, liver, lungs, and kidneys showed no histopathological abnormalities across all groups, indicating good biosafety (Supplementary Fig. 11). Immunohistochemistry (IHC) analysis further demonstrated a significant reduction in IL-17A expression across treatment groups, with the AcM-DDS group exhibiting the most pronounced suppression (Fig. 5j-k). All of these results indicate that AcM-DDS effectively attenuates systemic inflammation and mitigates splenic immune activation in the IMQ-induced PO model.

AcM-DDS ameliorates joint inflammation and bone erosion in a CIA mouse model of RA

Given the diverse types of AID and the limitations of the IMQ-induced PO model as an acute inflammation model, evaluating the efficacy of the AcM-DDS system in chronic autoimmune settings remains challenging. The CIA mouse model, a well-established model for RA research, induces an autoimmune response against type II collagen, leading to chronic joint inflammation, progressive cartilage degradation, and bone erosion[53]. Here, we used the CIA-induced mouse RA model to investigate the application of the AcM-DDS in the treatment of chronic autoimmune diseases. To establish this model, male DBA/1 J mice were immunized twice via tail injection of a collagen-Freund's adjuvant emulsion, with a two-week interval between immunizations. One week after the initial immunization, mice were assigned to the same treatment groups and dosing regimen as in the IMQ model, receiving retro-orbital venous injections every 10 days for one month (Fig. 6a). IVIS imaging revealed that, compared with DiD-mBMSC, retro-orbital injection of DiD-CD4-mBMSC resulted in preferential accumulation in the limbs and inflammatory regions of CIA mice within 24 h (Supplementary Fig. 12). Throughout the study, all groups exhibited stable weight gain (Supplementary Fig. 13a). By day 18 post-immunization, the Model group developed limb swelling, with 5 out of 6 mice displaying pronounced joint inflammation at the study endpoint. The mBMSC group exhibited early-stage swelling with lower severity, resulting in a final incidence of 3/6. In the CdgLipo group, inflammation onset was delayed until day 28; however, by the endpoint, 4/6 mice exhibited severe joint swelling, aligning with the limited clinical efficacy of IL-17A monoclonal antibodies in RA treatment. The CD4-mBMSC group displayed a milder disease phenotype, with arthritis incidence limited to 2/6 mice. Notably, AcM-DDS treatment significantly attenuated disease progression, with only 1/6 mice exhibiting mild inflammation at the endpoint (Fig. 6b).

Micro-CT analysis of hind limb joints (knee, ankle, and foot) revealed severe bone erosion and structural degradation in the Model group (Fig. 6c). The CdgLipo group exhibited notable but less severe bone loss, whereas the mBMSC group showed minimal knee cartilage destruction but substantial foot bone erosion. The CD4-mBMSC group demonstrated improved joint integrity compared to mBMSC, while the AcM-DDS group exhibited near-intact bone structures, comparable to the Sham group. Three-dimensional quantitative analysis of the subchondral bone in the knee joint revealed significant improvements

https://doi.org/10.1038/s41467-025-67698-1

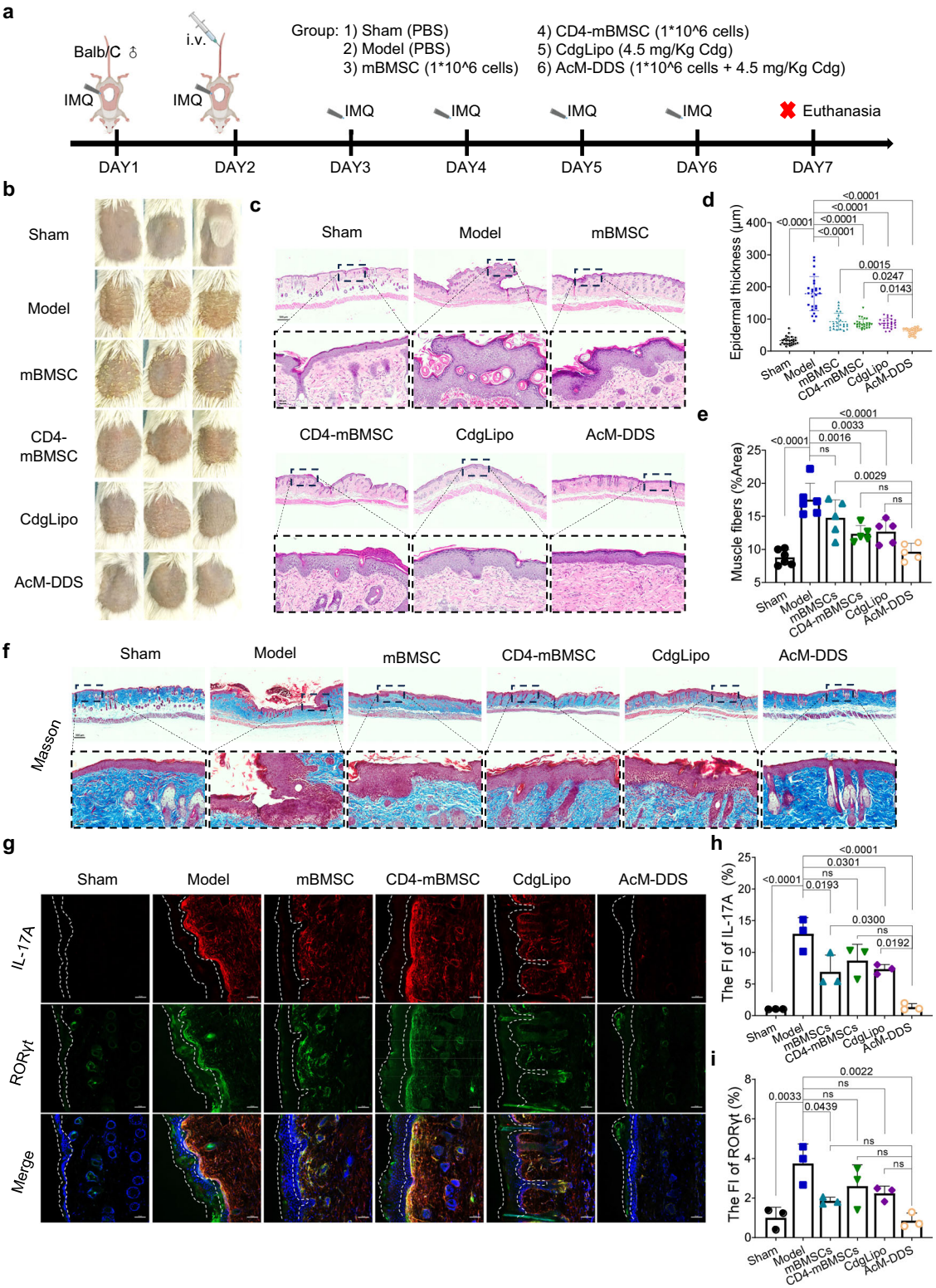

in bone volume fraction (BV/TV), structural model index (SMI), and trabecular number (Tb. N) parameters in all mBMSC-based treatment groups, while the CdgLipo group showed no apparent recovery (Fig. 6d, e, Supplementary Fig. 13b, c). Histological analysis of decalcified knee (Supplementary Fig. 13d) and ankle (Supplementary Fig. 13e) joints sections via H&E staining further supported these findings. Both the Model and CdgLipo groups displayed evident synovial inflammation, cartilage degradation and subchondral bone damage. Toluidine blue staining of knee joints (Fig. 6f, g) and safranin-O/fast green staining of ankle joints (Fig. 6h, i) revealed varying degrees of cartilage degeneration among mBMSC-based treatment groups. Noticeable loss of acidic glycosaminoglycans was observed in the mBMSC group, indicating evident cartilage degradation. The CD4-mBMSC group also showed signs of cartilage degeneration, but to a lesser extent compared with the mBMSC group, suggesting partial chondroprotection. In contrast, the AcM-DDS group exhibited well-preserved cartilage structure and proteoglycan content, showing the most pronounced protective effect among all treatments.

Fig. 4 | AcM-DDS alleviates IMQ-induced psoriasiform dermatitis by inhibiting Th17 differentiation. a Schematic representation of treatment groups and administration strategy. Eight-week-old, 30 male BALB/c mice (n = 5 for all groups) were used. Created in BioRender. Li, J. (2026) https://BioRender.com/rmjk4bf. **b** Representative images of dorsal skin morphology across different treatment groups in the DAY7. n = 5 mice per group. **c** H&E-stained paraffin sections of dorsal skin from each group. Scale bars, 500 μm or 50 μm. n = 5 mice per group. **d** Quantification of epidermal thickness based on H&E staining. Each mouse is assessed at five different sites. n = 5 randomly selected fields from five mice. **e** Quantification of muscle fiber area derived from Masson' s trichrome staining. n = 5 per group. **f** Masson' s trichrome staining of dorsal skin sections from each group. Scale bars, 500 μm or 50 μm. n = 5 mice per group. **g** Representative images of IL-17A and RORγt dual IF staining in dorsal skin frozen sections. The area between the two dashed lines represents the epidermal layer of the skin. Scale bars, 50 μm. **h** Quantification of IL-17A fluorescence intensity (FI), normalized to the Sham group. *n* = 3 mice per group. **i** Quantification of RORγt fluorescence intensity, normalized to the Sham group. *n* = 3 mice per group. ns = no significance. Data are presented as means ± SD and are analyzed by one-way ANOVA followed by Tukey's multiple comparisons test (**d**, **f**, **h**- **i**). Source data are provided as Source Data file.

AcM-DDS reduces inflammatory marker expression in knee joints and spleens of CIA mice

RA differs from PO in pathogenesis. Whereas PO is primarily driven by Th17 cell-mediated inflammation, RA involves a more complex immune network[54,55]. In addition to IL-17A, TNF and IL-6 drive synovial inflammation and joint destruction[55]. Moreover, MMP3 accelerates cartilage degradation by breaking down the extracellular matrix, exacerbating joint damage[56]. To further elucidate the differential therapeutic effects among treatment groups, we performed IHC analysis of CD4 (Fig. 7a), IL-17A (Supplementary Fig. 14a), RORγt (Supplementary Fig. 14b), TNF (Fig. 7b), IL-6 (Fig. 7c), and MMP3 (Fig. 7d) in knee joint paraffin sections of CIA model mice. Compared with the Model, CD4 expression was significantly reduced in the mBMSC, CD4-mBMSC, and CdgLipo groups, with no notable differences among them. In contrast, AcM-DDS treatment nearly abolished their expression (Fig. 7e). Similarly, IL-17A and RORγt levels were significantly lower in all four treatment groups compared to the Model group, though no significant differences were observed among them, indicating robust suppression of Th17 cell differentiation (supplementary Fig. 14c, d). In contrast, TNF and IL-6 exhibited distinct expression patterns. While CdgLipo failed to suppress TNF, CD4-mBMSC showed greater inhibitory effects than mBMSC, comparable to AcM-DDS (Fig. 7f). Similarly, IL-6 expression persisted to some extent in the mBMSC, CD4-mBMSC, and CdgLipo groups but was nearly undetectable in the AcM-DDS group (Fig. 7g). For MMP3, CdgLipo had minimal impact on MMP3 expression, whereas mBMSC, CD4-mBMSC, and AcM-DDS effectively suppressed MMP3 expression (Fig. 7h). These findings suggest that variations in inflammatory cytokine regulation among treatment groups may underlie differences in therapeutic efficacy.

Furthermore, we assessed the proportion of Th17 ($CD4^+IL\text{-}17A^+$) cells in splenic tissues using flow cytometry. Compared to the Model group (24.9%), the proportion of Th17 cells was significantly reduced in the mBMSC (8.5%), CD4-mBMSC (11.5%), CdgLipo (11.4%), and AcM-DDS (7.37%) groups, with levels comparable to the Sham group (5.50%) (Fig. 7i, supplementary Fig. 14e). In situ IF staining for CD4, RORγt, and IL-17A in frozen spleen sections further corroborated the flow cytometry findings (Fig. 7j, supplementary Fig. 14f). Considering the potential safety concerns associated with long-term administration, serum biochemical analyses were performed to evaluate hepatic and renal function (ALT, AST, γ-GT, UREA, CREA, and UA). All parameters remained within normal ranges across groups (supplementary Fig. 15a). Moreover, H&E staining of paraffin-embedded sections of the heart, liver, lung, and kidney (supplementary Fig. 15b), as well as the jejunum and colon (supplementary Fig. 16), revealed no apparent pathological alterations, indicating that these treatments did not induce organ toxicity. These results collectively demonstrate that AcM-DDS effectively suppresses systemic Th17 differentiation, thereby mitigating inflammation both in the spleen and at the joint level, ultimately contributing to the attenuation of RA pathogenesis.

Discussion

MSCs hold significant potential for AID treatment due to their dual properties of immunoregulation and tissue repair. However, a major challenge in intravenous infusion is the poor homing efficiency of MSCs to target sites. In this study, we develop an AcM-DDS using bioorthogonal chemistry to gently attach antibodies to the MSC surface, thereby enhancing their targeting capability. This conjugation strategy, widely used in ADC, has demonstrated systemic safety in clinical settings, supporting the translational potential of antibody-conjugated MSC.

Specifically, antibodies targeting $CD4^+$ T cells—central players in the pathogenesis of AID[34]—were conjugated to BMSC. In vivo imaging system analysis revealed a sixfold increase in the homing efficiency of CD4-BMSC to the inflammatory lesions in PO mice. Although CD4 is broadly expressed among helper T-cell subsets, our in vivo data indicate that AcM-DDS preferentially accumulates in inflamed tissues enriched with activated $CD4^+$ T cells, where Th17 cells predominate (Supplementary Fig. 1). As naïve $CD4^+$ T cells are relatively limited in inflamed sites, their potential engagement by AcM-DDS is expected to be limited. Consistent with this, no apparent immunological side effects or abnormal immune activation were observed in either the RA or PO models following repeated administration. Moreover, since MSCs are inherently immunomodulatory and non-cytotoxic, transient interactions with non-activated $CD4^+$ T cells are unlikely to cause adverse immune responses.

In future work, coupling BMSC with therapeutic antibodies such as IL-17R monoclonal antibodies[57] could leverage the therapeutic potential of the antibodies themselves, thereby achieving a synergistic therapeutic effect. This strategy addresses the fundamental issue of low MSC homing efficiency while opening avenues for enhanced MSC-based therapies through synergistic antibody conjugation technologies.

In addition to enhancing BMSC accumulation at inflamed sites, antibody-conjugated BMSC can also enable targeted delivery of small-molecule drugs. RORγt, a nuclear receptor critical for Th17 differentiation and IL-17A secretion, is an attractive but challenging target due to off-target effects arising from structural similarities with RORα and RORβ[39,46,58,59]. In this study, we encapsulated Cdg, a RORγt inverse agonist that failed in Phase II clinical trials[47], within liposomes and utilized CD4-mBMSC for targeted intracellular delivery. This approach not only enhances the capacity of AcM-DDS to inhibit Th17 cell differentiation but also offers a promising strategy for the selective delivery of RORγt inverse agonists. By directing the drug specifically to the inflamed tissues, this method mitigates the off-target inhibition of non-specific ROR nuclear receptors, thus improving the precision and efficacy of the treatment.

Cdg previously showed unfavorable systemic exposure and metabolic instability in preclinical studies, including body weight loss and gastrointestinal toxicity observed in a 39-week dog study[47]. Th17 cells are essential for intestinal homeostasis by producing IL-17 and IL-22, which maintain epithelial barrier integrity[60]. Chronic inhibition of Th17 cells may disrupt this balance and cause mucosal injury. In our short-term models (1-5 weeks), histological analyses revealed no intestinal damage in either the CdgLipo or AcM-DDS groups. These findings suggest that, in our models, AcM-DDS primarily enhances local Cdg efficacy at inflammatory sites rather than reducing gastrointestinal side effects.

https://doi.org/10.1038/s41467-025-67698-1

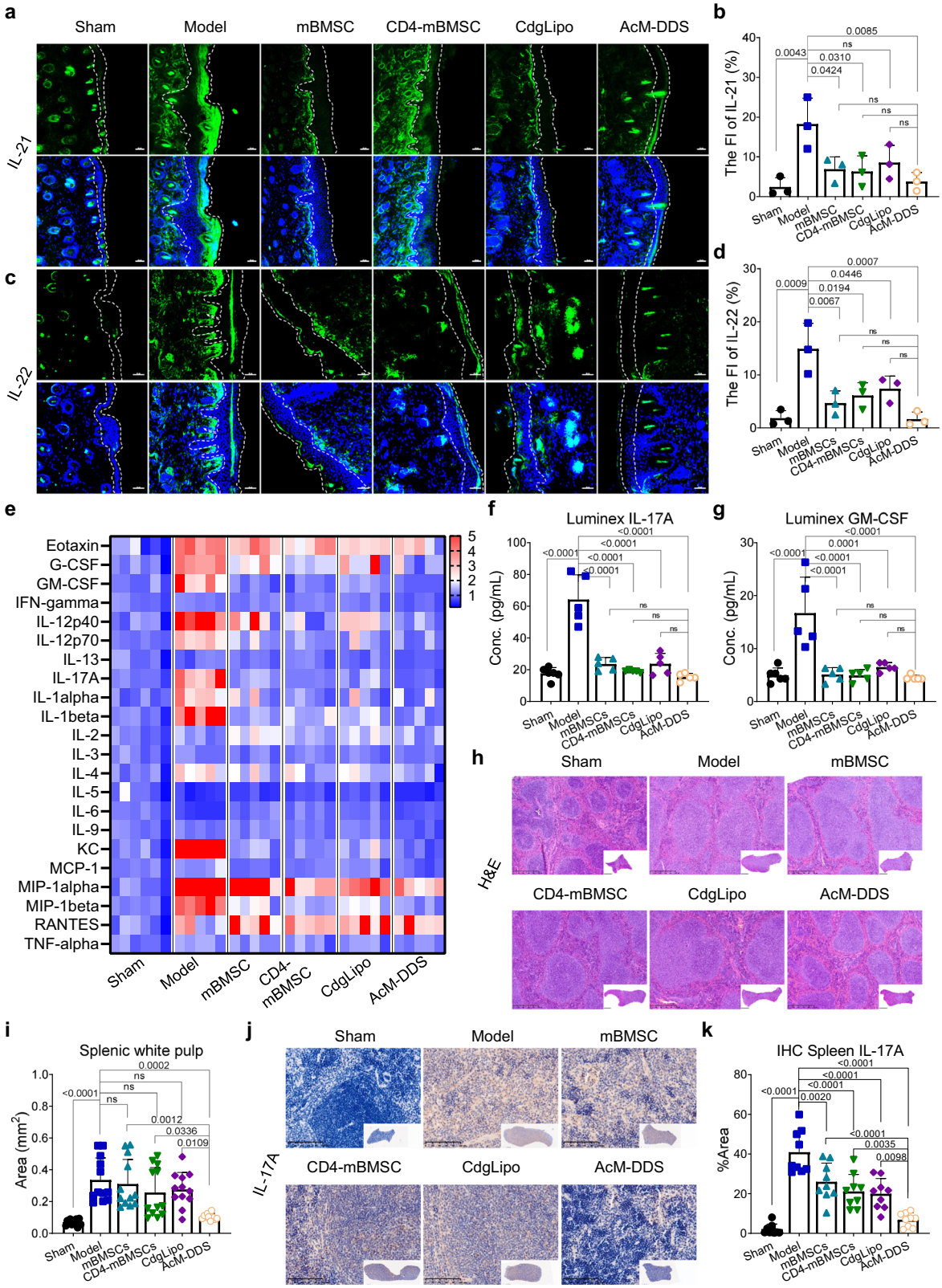

Fig. 5 | AcM-DDS suppresses inflammatory cytokines in IMQ-induced PO mice. **a** Representative IF images of IL-21 in dorsal skin cryosections. Scale bars, 50 μm. **b** Quantification of IL-21 fluorescence intensity. $n = 3$ mice per group. **c** Representative IF images of IL-22 in dorsal skin cryosections. Scale bars, 50 μm. **d** Quantification of IL-22 fluorescence intensity. n = 3 mice per group. **e** Heatmap of 22 inflammatory cytokines in dorsal skin, analyzed via Luminex assay. n = 5 mice per group. Luminex-based quantification of IL-17A (**f**) and GM-CSF (**g**). **h** Representative H&E-stained images of spleen paraffin sections. Scale bars, 500 μm. **i** Quantification of splenic white pulp area. $n = 12$ fields per group. **j** Representative IHC images of IL-17A in spleen. Scale bars, 100 μm. **k** Quantification of IL-17A expression in spleens. $n = 9$ per group with 4 mice and two independent experiments. Data are presented as means ± SD and are analyzed by one-way ANOVA followed by Tukey's multiple comparisons test (**b**, **d**, **f**, **g**, **i**, **k**). ns = no significance. Source data are provided as Source Data file.

https://doi.org/10.1038/s41467-025-67698-1

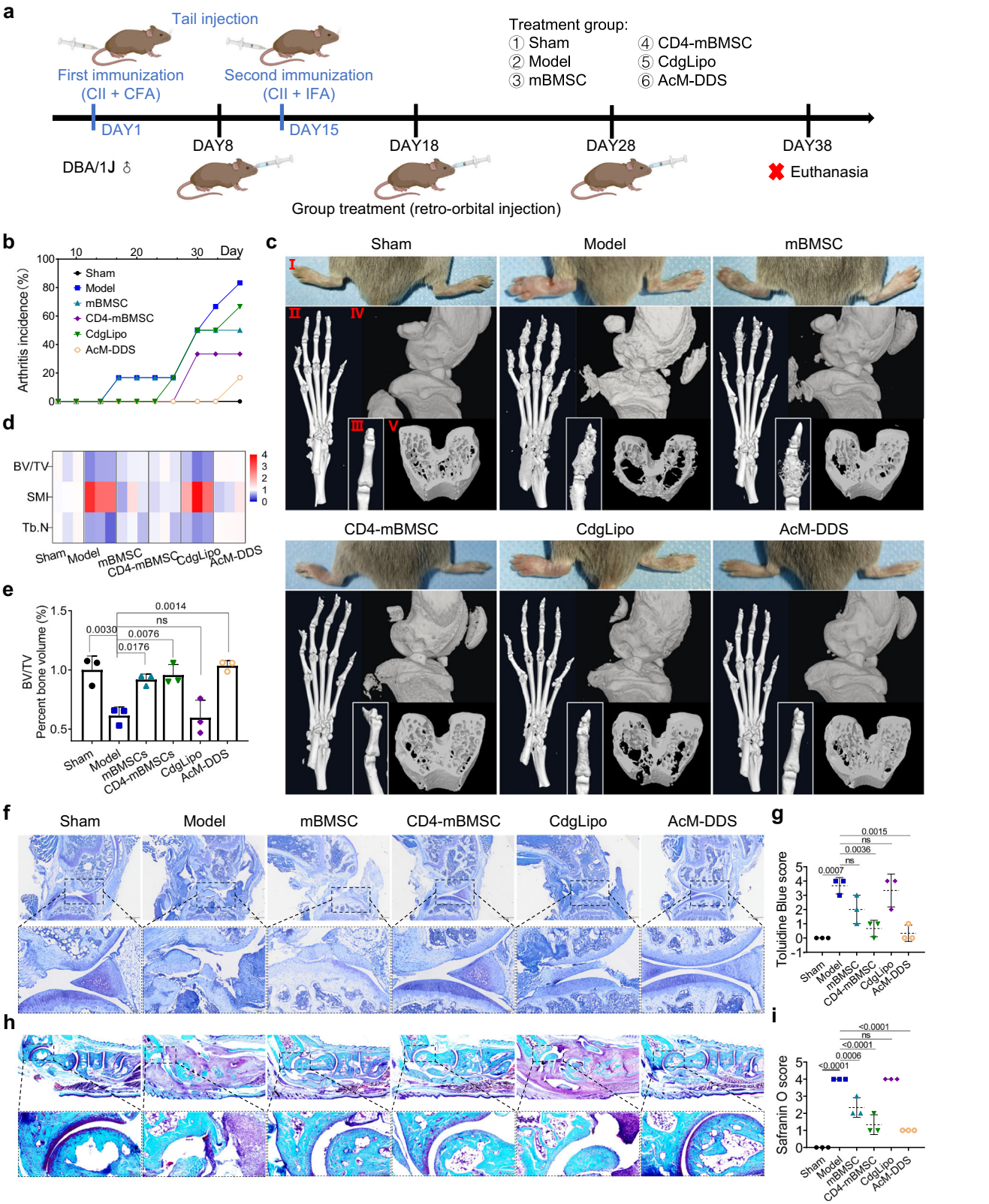

Fig. 6 | Therapeutic evaluation of AcM-DDS in a CIA mouse model of RA. **a** Schematic of CIA induction, treatment regimen, and experimental timeline. Six to seven-weeks-old, 36 male DBA/1J mice (n = 6 mice per group) were used. Created in BioRender. Li, J. (2026) https://BioRender.com/rmjk4bf. **b** Arthritis incidence over time in each group. **c** Representative images of hind limb swelling at the study endpoint (I), and Micro-CT 3D reconstructions of knee and ankle joints: II, foot and ankle; III, toes; IV, knee; V, subchondral bone sections. **d** 3D heatmaps of subchondral bone microarchitecture: Tb.N, SMI and BV/TV. **e** Quantification of BV/TV. $n = 3$ mice per group. Toluidine staining of decalcified knee joint sections (**f**) and corresponding histological scores (**g**). $n = 3$ mice per group. Scale bars, 200 μm or 50 μm. Safranin O-Fast green staining of decalcified ankle joint sections (**h**) and scoring (**i**) for cartilage integrity. $n = 3$ mice per group. Scale bars, 500 μm (overview) or 100 μm (magnified view). Data are presented as means ± SD and are analyzed by one-way ANOVA followed by Tukey's multiple comparisons test (**e**, **g**, **i**). ns no significance. Source data are provided as Source Data file.

https://doi.org/10.1038/s41467-025-67698-1

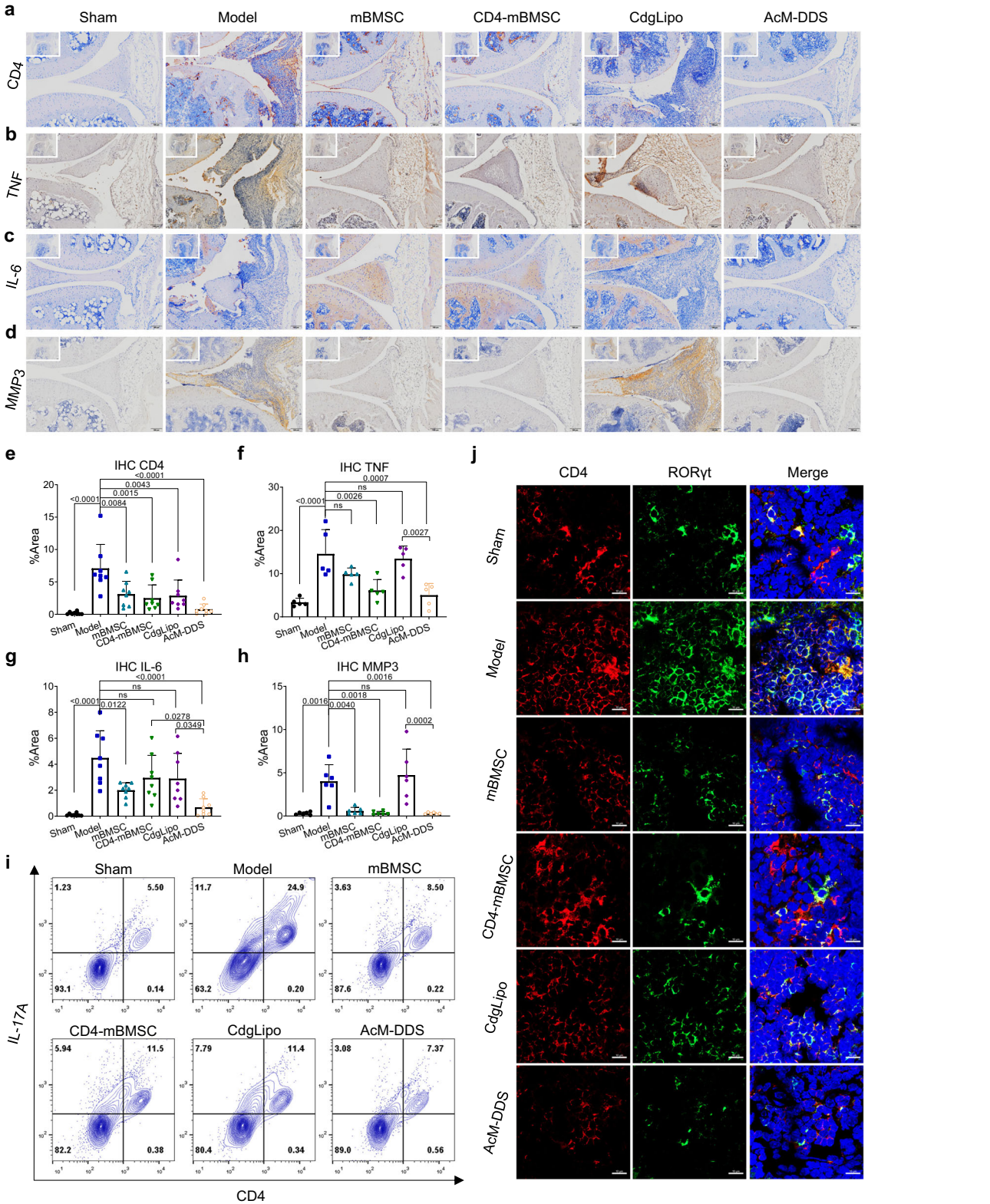

Fig. 7 | AcM-DDS suppresses inflammatory cytokine in the knee joint and spleen of CIA mice. Representative IHC staining of CD4 (**a**), TNF (**b**), IL-6 (**c**), and MMP3 (**d**) in paraffin-embedded knee joint sections, with magnified views of the articular surface and corresponding whole-section images in the top-left corners. Scale bars, 200 μm or 100 μm. Quantification of IHC staining for CD4 (**e**), TNF (**f**), IL-6 (**g**), and MMP3 (**h**). For CD4 and IL-6 (**e**, **g**), n = 8 fields from 4 mice per group. For TNF (**f**), *n* = 5 mice per group. For MMP3 (**h**), *n* = 6 mice per group. **i** Flow cytometry analysis of CD4 and IL-17A co-expression in splenic cells from each group. *n* = 3 mice per group. Gating strategy are shown in Supplementary Fig. 14e. **j** Confocal microscopy images of in situ CD4 and RORγt co-staining in spleen sections. Scale bars, 10 μm. *n* = 3 mice per group. Data are presented as means ± SD and are analyzed by one-way ANOVA followed by Tukey's multiple comparisons test (**e**–**h**). ns no significance. Source data are provided as a Source Data file.

Compared to ADC-based delivery of RORγt inverse agonists, AcM-DDS offers a broader selection of targeting antibodies, as it is not limited to receptors capable of mediating endocytosis. While ADCs require binding to membrane receptors that can trigger receptor-mediated internalization to deliver and release the payload intracellularly, not all receptors possess this function. In contrast, AcM-DDS can target any membrane protein, enabling more flexible drug delivery. The AcM-DDS system was designed to enrich the local concentration of Cdg around $CD4^+$ T cells rather than to achieve cell-internal release as in ADC therapeutics. In vitro release assay showed that approximately 25% of the payload was released within 24 h, indicating that limited diffusion occurs before complete tissue homing. In our study, we attempted to evaluate drug release in circulation, but the low drug loading in MSCs made it technically challenging to quantify drug concentrations in blood and tissues. Even with LC-MS analysis, the sensitivity of current methods was insufficient to reliably detect the low drug levels present. Therefore, we acknowledge that unintended partial release cannot be entirely excluded. A major direction for future optimization is to ensure that nanoparticles are released from MSC carriers only after tissue homing. To minimize premature drug release from intracellularly loaded MSC and ensure post-homing release, feasible strategies include inducible CRISPRi/siRNA-mediated repression of ABC transporters or engineering MSC for inflammation-triggered exocytosis.

The therapeutic efficacy of the AcM-DDS system was evaluated in two mouse models of AID: the IMQ-induced PO model and the collagen-induced RA model. Results demonstrated that AcM-DDS successfully integrates the therapeutic advantages of BMSC and Cdg, yielding substantial improvements in both models. Specifically, AcM-DDS suppressed Th17 cell differentiation and downregulated multiple pro-inflammatory cytokines, conferring protective effects on skin, cartilage, and bone. In the PO model, CD4-mBMSC exhibited greater efficacy than mBMSC alone, while the CdgLipo group demonstrated pronounced therapeutic benefits. In RA, however, CdgLipo alone offered limited bone protection despite comparable suppression of IL-$17A^+CD4^+$ T cells, reflecting the multifactorial nature of RA pathogenesis driven by IL-6 and TNF[55]. This aligns with the clinical failure of IL-17A monoclonal antibodies in RA[61]. In contrast, AcM-DDS effectively suppressed IL-17A, IL-6, and TNF, indicating its broader immunomodulatory capacity.

The safety profile of AcM-DDS is primarily determined by the biodistribution of MSC and the localization of encapsulated drugs. By enriching BMSC and Cdg at inflammatory sites, AcM-DDS enhances local therapeutic effects without increasing systemic toxicity. Although high local concentrations may require dose optimization, no tissue damage or inflammatory exacerbation was observed in the current dosing regimen.

Beyond AID, this system shows broad translational potential for a range of immune-mediated disorders. In December 2024, Ryoncil became the first MSC-based therapy approved by the U.S. Food and Drug Administration (FDA) for the systemic treatment of acute graft-versus-host disease (aGVHD) in pediatric patients[62]. Shortly thereafter, in January 2025, China approved Amimestrocel, its first MSC-based therapy, also indicated for systemic administration in aGVHD treatment. These milestones underscore the versatility of MSC-based therapies in modulating immune responses. Leveraging its capacity for targeted immune modulation, the AcM-DDS system represents a promising therapeutic platform for addressing other immune-mediated disorders, including aGVHD and atopic dermatitis, further highlighting its potential for broad applications in immune modulation and systemic therapy.

Together, our AcM-DDS platform enables targeted delivery of BMSC to inflammatory sites in AID through antibody conjugation, allowing both the cells and their small molecule payloads to act specifically at disease sites. This strategy not only enhances the therapeutic efficacy of BMSC themselves but also enables synergistic effects with co-delivered small molecule drugs. Compared to genetically engineered BMSC that overexpress targeting receptors, antibody-conjugated BMSC achieve similar targeting capability with improved safety. Furthermore, unlike traditional ADCs, AcM-DDS offers broader target selection by not being limited to internalizing receptors, allowing for more precise delivery of small molecules. Thus, AcM-DDS represents a versatile and promising drug delivery technology for the treatment of AIDs.

The AcM-DDS platform demonstrates considerable translational potential as a next-generation MSC-based therapy. The antibody-conjugated MSC component is technically straightforward, and similar antibody-tagged immune cell therapies, such as NK and γδT cells, are already under clinical development (Acepodia Biotech, Inc.). Using a clinically approved CD4 antibody (Ibalizumab) provides a favorable safety and regulatory profile. While antibody conjugation and small-molecule loading add modest processing complexity, these steps do not substantially increase production costs, as cell manufacturing remains the major expense in MSC-based therapies. Moreover, enhanced homing efficiency enables equivalent or superior efficacy with markedly fewer cells, potentially lowering overall treatment costs. AcM-DDS retains the native differentiation and viability of MSC but is not suitable for long-term culture or multiple passages; drug-loaded cells should be freshly prepared due to gradual payload diffusion after ~24 h. Limitations of the present study include the use of murine MSC and preclinical models that do not fully recapitulate human immune complexity. Future optimization could involve antibodies with higher cellular specificity, such as those targeting Th17-, Th1-, or Th2-related markers, to refine delivery precision. Furthermore, scaling the current laboratory process to pilot or GMP production will be required for clinical translation. Substituting Cedirogant with an FDA-approved small molecule would further enhance the clinical readiness of this adaptable cell-based delivery platform.

Methods

Cell culture

C57BL/6 mouse bone marrow MSC (mBMSC) were purchased from Oricell (Oricellbio, cat# MUBMX-01001, CN). The mBMSC were cultured in αMEM medium (Gibco, cat#C12571500, USA) supplemented with 10% fetal bovine serum (Hyclone, cat#SV30208.02, USA), 1% Penicillin-Streptomycin solution (Gibco, cat#15140122, USA), 1 ng/mL murine FGF-basic protein (Peprotech, cat#450-33, USA), and 1% GlutaMAX (Gibco, cat#07946, USA).

Preparation of CD4 monoclonal antibody conjugated mBMSC (CD4-mBMSC)

To prepare the DBCO-modified antibody, 15 μg of CD4 monoclonal antibody (Invitrogen, cat#14-0041-85, USA) was reacted with 69 μg of DBCO-PEG_4-NHS ester (Confluore, cat#BCD-7, CN) in 1 mL PBS under gentle stirring (200 rpm) at 4 °C overnight. The following day, the reaction mixture was centrifuged using a 100 kDa ultrafiltration device (Millipore, cat#UFC5100096, GER) to remove any unreacted DBCO-PEG_4-NHS ester, yielding DBCO-CD4mAb. Similarly, DBCO-PEG_4-NHS ester was conjugated with FITC-labeled CD4 monoclonal antibody (eBioscience, cat#11-0041-82, USA) under the same conditions to obtain DBCO-FITC-CD4mAb.

For cell surface modification, 1×10^6 mBMSC were incubated overnight with 6 mL of 10 μM N-azidoacetylmannosamine-tetraacylated (Ac_4ManNAz) (MCE, cat#HY-W728531, USA). The next day, cells were treated with 1 mL of 100 nM DBCO-FAM (Confluore, cat#BF-11, CN), DBCO-CD4mAb, or DBCO-FITC-CD4mAb and incubated at 37 °C for 30 min. Afterward, stain the nuclei with Hoechst33342 (Beyotime, cat#C1027, CN) and observe the fluorescence on the cell membranes using a confocal fluorescence microscope (ZEISS, LSM900, Germany). The number of antibodies anchored

on each cell was further quantified by flow cytometry using Accu-Check™ ERF reference beads (Invitrogen, cat#A55950, USA), revealing that approximately 2,500 antibody molecules were conjugated per cell on average.

Formulation and characterization of Cedirogant-loaded liposome (CdgLipo)

Dissolve 1,2-Dipalmitoyl-rac-glycero-3-phosphocholine (Aladdin, cat#D353387, CN), cholesterol (Aladdin, cat#C104028, CN), DSPE-PEG2000 (Melopeg, cat#070701, CN), and Cedirogant (Hifuture, cat#2055496-11-0, CN) in dichloromethane in a mass ratio of 6:2:2:1. Remove the dichloromethane by rotary evaporation under reduced pressure to form a thin film. Hydrate the film by adding PBS and sonicating at 42 °C for 30 minutes to obtain CdgLipo. To prepare Cy5-CdgLipo, add 0.15 mass ratio of lipophilic Cy5 (Aladdin, C266403#, CN) to the formulation and follow the same procedure.

To assess drug loading and encapsulation efficiency, mix 100 μL of Cy5-CdgLipo with 900 μL of acetonitrile, then centrifuge and analyze the supernatant using HPLC (SHIMADZU, LC-20ADxr, JP). Determine the particle size and zeta potential of the liposomes using a Malvern particle size analyzer (Malvern, ZETASIZER NANO ZS, UK). Evaluate the size and particle number of the liposomes using Nano-Flow Cytometry (NanoFCM, cat#N30E, CN). Capture the morphology of the liposomes with transmission electron microscopy (TEM, G2 Spirit Biotwin, CN) imaging.

Construction of AcM-DDS

To construct the AcM-DDS, 50 μL of CdgLipo suspension (2 mg/mL Cdg, approximately 9.55E + 10 particles) was added to 1 mL of α-MEM complete medium and co-incubated with CD4-mBMSC for 1 h. After incubation, the cells were washed three times with PBS and counted to obtain the AcM-DDS construct. The Cdg uptake efficiency was quantified by collecting the culture supernatant and lysing the cells with acetonitrile, followed by HPLC analysis, which indicated that approximately 90 μg of Cdg was internalized per 1×10^6 cells. Furthermore, based on the particle number obtained from Nano-Flow analysis, a linear correlation between the fluorescence intensity of Cy5-labeled CdgLipo and Cdg content was established, allowing the estimation that each CD4-mBMSC internalized approximately 1.15×10^4 CdgLipo particles on average.

Animals

Eight-week-old, male BALB/c mice (n = 80, cat#BSTSC-013) were purchased from BesTest Bio-Tech (Zhuhai, CN). Six to seven-weeks-old, male DBA/1J mice (n = 80, cat# N000219) were purchased from GemPharmatech (Foshan, CN). All mice were kept in a specific pathogen-free (SPF) animal facility at Shenzhen Institute of Advanced Technology, Chinese Academy of Sciences. Mice were accommodated in group housing under conditions of 20–24 °C temperature and 40–60% humidity, following a 12-hour light/12-hour dark cycle. Mice were fed a standard chow diet (Keao, cat#12231, CN) with ad libitum access to food and water. Experimental and control mice were housed in separate cages but within the same rack and environmental conditions, without cross-contact between groups. Euthanasia was performed by CO_2 inhalation followed by cervical dislocation.

IMQ-induced PO mouse model

Male BALB/c mice were used to establish the imiquimod (IMQ)-induced psoriasis-like (PO) model. Under isoflurane anesthesia, a 2.5 × 2.5 cm area of dorsal fur was removed using depilatory cream and thoroughly cleaned. Beginning the following day, IMQ cream (MED-SHINE, CN) was applied daily to the depilated area for seven consecutive days to induce psoriatic inflammation, while the Sham group received Vaseline.

Two independent experiments were conducted. In the first experiment, mice were randomly assigned to six groups ($n = 5$ per group): Sham, Model, mBMSC, CD4-mBMSC, CdgLipo, and AcM-DDS. Starting on Day 2, treatments were administered intravenously as follows: mBMSC or CD4-mBMSC (1×10^6 cells in 200 μL suspension), CdgLipo (4.5 mg/kg Cdg), or AcM-DDS (1×10^6 CD4-mBMSC preloaded with 4.5 mg/kg Cdg liposomes). Sham and Model groups received equivalent volumes of saline. On Day 7, mice were euthanized, and their affected skin and internal organs were collected for subsequent analysis.

In the second experiment, a separate cohort of IMQ-induced mice was used to further evaluate the pharmacological efficacy and dosing schedule of free and liposomal Cdg formulations. Mice were divided into five groups: Sham ($n = 3$), Model ($n = 3$), MTX (positive control, $n = 5$), Cdg ($n = 5$), and CdgLipo ($n = 5$). MTX was administered daily via oral gavage at 1 mg/kg in a carboxymethylcellulose sodium (CMC-Na) vehicle. Cdg was delivered as a single intravenous injection on Day 2 (4.5 mg/kg), whereas CdgLipo was administered intravenously on Days 2 and 5 (4.5 mg/kg per injection). Sham and Model groups received saline or Vaseline, respectively. All other experimental conditions, including IMQ application, euthanasia, and tissue collection, were identical to those in the first experiment.

Mouse model of collagen-induced arthritis

The CIA mouse model was established following the method previously reported[63]. Thirty-six male DBA/1J mice were randomly divided into six groups, with six mice in each group, according to the grouping scheme used for psoriasis mice. For the initial immunization, bovine type II collagen (Chondrex, cat#20020, USA) emulsified with complete Freund's adjuvant (Chondrex, cat#7001, USA) was subcutaneously injected into the base of the tail at a dose of 100 μL per mouse, while the Sham group received an equal volume of saline. Fourteen days later, a booster immunization was administered using type II collagen emulsified with incomplete Freund's adjuvant (Chondrex, cat#7002, USA). Treatment was initiated one week after the initial immunization, following the same dosing regimen as the psoriasis mouse model. Subsequent immunizations were administered every ten days, for a total of three immunizations. At the end of the experiment, blood, spleen, lymph nodes, and knee joints were collected from the mice.

Biodistribution of CD4-mBMSC

Label 1×10^6 mBMSC or CD4-mBMSC with 10 μM DiD cell membrane dye (Invitrogen, cat#V22887, USA). The labeled cells were injected into IMQ-induced PO mice via the tail vein or into CIA mice via retro-orbital venous injection. Whole-body fluorescence images were acquired at different time points post-injection using an in vivo imaging system (IVIS Spectrum, PerkinElmer, USA) to monitor the biodistribution of the transplanted cells.

Binding ability of CD4-mBMSC with $CD4^+$ T cells

A single 8-week-old male BALB/c mouse was euthanized, and its spleen was harvested. The spleen was mechanically dissociated to obtain splenocytes, which were subsequently subjected to magnetic bead-based sorting for $CD4^+$ T cell isolation (STEMCELL, cat#19852A, CAN) according to the manufacturer's protocol. To assess sorting efficiency, 100,000 cells were stained with FITC-CD4 monoclonal antibody and analyzed by flow cytometry (Easycell, WELLGROW, CN) to determine the proportion of $CD4^+$ T cells. For co-culture experiments, $CD4^+$ T cells were suspended and incubated with pre-seeded, Dil-labeled CD4-mBMSC for 3 hours. Following incubation, all culture media were removed, and the cells were gently washed with PBS. Nuclei were then counterstained with Hoechst 33342 (Beyotime, cat# C1022, CN), and cell binding interactions were visualized using confocal microscopy.

Luminex cytokines assay

After euthanizing the mice, the inflamed skin area was collected in a sterile environment. The samples were washed with PBS and rapidly frozen in liquid nitrogen. These samples were then sent to Shanghai Huaying Biomedical Technology Co., Ltd. for protein extraction and cytokines concentration test. Protein quantification was performed using the BCA assay. The Luminex 2000 system (Luminex Corporation, Austin, USA) was employed to measure the expression levels of Eotaxin, G-CSF, GM-CSF, IFN-γ, IL-12p40, IL-12p70, IL-13, IL-17A, IL-1α, IL-1β, IL-2, IL-3, IL-4, IL-5, IL-6, IL-9, KC, MCP-1, MIP-1α, MIP-1β, RANTES, and TNF in the samples.

Osteogenic, adipogenic, and chondrogenic Differentiation of mBMSC-based group

Four groups of cells were used for differentiation assays: mBMSC, CdgLipo-mBMSC (mBMSC pre-loaded with CdgLipo), CD4-mBMSC, and AcM-DDS.

For osteogenic induction, an osteogenic induction medium consisting of 100 nM dexamethasone (Sigma-Aldrich, cat#D4902, USA), 10 mM β-glycerophosphate disodium salt hydrate (Sigma-Aldrich, cat#G9422, USA), and 50 μg/mL vitamin C (Sigma-Aldrich, cat#A8960, USA), all formulated in αMEM complete medium and filtered for sterilization. Seed mBMSC at a density of 1 × 10^5 cells per well in a 6-well plate (Corning, cat#3516, USA) with 2 mL of normal complete medium per well. When cells reach 90% confluence, switch to osteogenic induction medium, refreshing it with new induction medium every two days. Continue the induction for 14 to 21 days. Fix cells using 4% paraformaldehyde solution (Beyotime, cat#P0099, CN) and proceed with staining using 1% Alizarin Red (Aladdin, cat#A100195, CN) or ALP staining (Beyotime, cat#P0321, CN).

For adipogenic differentiation, an adipogenic induction medium (OriCell, cat#MUXMX-90031, CN) was used according to the manufacturer's instructions. After 28 days of induction, cells were fixed and stained with Oil Red O (Sigma, cat#O0625, GER) to visualize intracellular lipid droplets.

For chondrogenic differentiation, 5×10^4 cells from each group were seeded into ultra-low attachment 96-well plates and cultured in chondrogenic induction medium (OriCell, cat#MUXMX-90041, CN) for 28 days. The resulting cartilage spheroids were fixed, cryoprotected with sucrose, embedded, and sectioned for Alcian Blue staining to evaluate glycosaminoglycan deposition.

Transcriptome sequencing

The mBMSC, CdgLipo-mBMSC, CD4-mBMSC, and AcM-DDS cell samples were collected and lysed using TRIzol reagent (Invitrogen, cat# 15-596-018, USA). Total RNA was extracted and subjected to bulk mRNA sequencing by BGI Genomics (Shenzhen, CN). Reads were quality-checked, filtered, and aligned to the mouse genome (mm10). Gene expression was quantified as FPKM, and differential expression between groups was analyzed using DESeq2 (FDR < 0.05). Functional enrichment analyses (GO and KEGG) were performed to interpret relevant biological processes.

CdgLipo uptake efficiency

Seed 4×10^5 mBMSC in a confocal culture dish. After Ac4ManNAz treatment and antibody coupling, stain the cells with Lysotracker Deep Red (Invitrogen, cat#L12492, USA), Mito-tracker Red (Invitrogen, cat#M22425, USA), and Hoechst 33342, and observe the staining using a confocal microscope. Immediately after, add Cy5-CdgLipo, and capture images after 2 minutes of uptake.

After incubating CD4-mBMSC with CdgLipo for one hour, the culture supernatant was collected, and the cells were trypsinized, counted, and lysed. The intracellular and supernatant Cdg concentrations were quantified using HPLC. The results indicated that the intracellular Cdg content reached 0.15 mg per million cells.

Cdg release efficiency from CDGLipo

To assess the release efficiency of Cdg from CdgLipo, 1 mg/mL CdgLipo was placed in a 3 kDa ultrafiltration membrane bag (Millipore, GER) and submerged in PBS under continuous stirring at 300 rpm. At designated time points (0, 1, 3, 5, 16, 24, 36, and 48 h), aliquots from the external PBS solution were collected, and the Cdg concentration was quantified using HPLC.

To evaluate the intracellular release kinetics of Cdg following cellular uptake, CD4-mBMSC were incubated with 1 mg/mL Cy5-CdgLipo for one hour, after which the medium was replaced with fresh culture medium. At 0, 1, 3, 5, 16, 24, 36, and 48 h, the culture supernatants were collected, and fluorescence intensity was measured using a microplate reader to quantify the extracellular release of Cy5-labeled Cdg.

Bio-TEM

Seed 1×10^6 mBMSC in a T25 flask. Following Ac4ManNAz treatment and antibody coupling, incubate the cells with CdgLipo for 1 hour. Detach with a cell scraper, centrifuge at 1100 x g for 5-10 minutes, and collect into a 1.5 mL microcentrifuge tube. Fix with 2.5% glutaraldehyde at 4 °C overnight. Discard the fixative, and wash three times with 0.1 M phosphate buffer (pH 7.0) for 15 minutes each. Subsequently, fix with 1% osmium tetroxide for 1-2 hours, then wash three times again with phosphate buffer. Dehydrate using a series of ethanol concentrations (30%, 50%, 70%, 80%, 90%, 95%), each for 15 minutes, followed by 100% ethanol for 20 minutes. Transition to pure acetone for 20 minutes. Infiltrate with a resin-acetone mixture (1:1) for 1 hour, a mixture (3:1) for 3 hours, then pure resin overnight. Cure the embedded samples at 70 °C overnight. Section the samples using a LEICA EM UC7 ultramicrotome into slices of 70-90 nm. Stain with lead citrate and saturated uranyl acetate in 50% ethanol for 5-10 minutes each. The sections are now ready for transmission electron microscopy observation and imaging.

Cell viability assay

To assess the viability of modified mBMSC, 5000 or 10000 mBMSC were seeded in 6-well plates and subjected to experimental treatments to generate CD4-mBMSC or AcM-DDS. Additionally, another group of mBMSC was incubated with CdgLipo for 1 hour, followed by drug removal. After 72 hours, cell viability was evaluated using the CCK-8 assay (GOONIE, cat#100-106, CN). Furthermore, to determine cell viability and apoptosis, cells were harvested, stained with Calcein-AM/7-AAD (Beyotime, cat#C2015M, CN), and analyzed by flow cytometry to distinguish live and dead cell populations.

Differential uptake and release of free Cy5 and Cy5-CdgLipo by N_3-mBMSC

To investigate the differences in uptake and release between N_3-mBMSC and mBMSC, both cell types were incubated with either free Cy5 (0.15 mg/mL) or an equivalent amount of Cy5 encapsulated in Cy5-CdgLipo for 1 hour. Following incubation, cells were digested and subjected to flow cytometry analysis to quantify intracellular Cy5 fluorescence intensity, reflecting the uptake efficiency.

For release kinetics, after a 1-hour uptake, cells were washed and replaced with fresh culture medium. At designated time points (0 h, 6 h, 24 h, and 48 h), cells were digested and analyzed via flow cytometry to measure Cy5 fluorescence intensity, providing a quantitative assessment of Cy5 release efficiency over time. Additionally, at 0 h, 24 h, and 48 h, confocal microscopy was used to capture in situ fluorescence images, providing a spatial visualization of Cy5 retention and release.

Efflux efficiency of Calcein in mBMSC and N_3-mBMSC after Verapamil treatment

To assess the efflux efficiency of calcein in mBMSC and N_3-mBMSC, cells were pretreated with verapamil (20 μM) for 4 hours. Following

treatment, cells were stained with calcein (5 μM) and Hoechst 33342 for 30 minutes. After staining, fluorescence intensity was monitored using confocal microscopy at 1 h, 6 h, and 12 h post-staining to evaluate the efflux dynamics of calcein. This experiment aims to determine the impact of verapamil on calcein retention and efflux efficiency in both cell types.

Micro-CT analysis of joint in CIA mice

Knee joints and ankle joints from CIA model mice in each treatment group were collected and fixed in neutral formalin for 24 hours, followed by ethanol fixation. Micro-CT scanning was performed using the Bruker μCT system (Skyscan 1276 Micro-CT, Kontich, Belgium) under the following parameters: voxel size of 6.5 μm (medium resolution), 70 kV, 200 mA, 0.25 mm Al filter, and an integration time of 350 ms. Three-dimensional reconstructions were generated from contoured two-dimensional images using a distance transformation-based algorithm within the CTvox software (version 3.3.0).

Histological staining

Skin and internal organs from IMQ mice, as well as knee and ankle joints and internal organs from CIA mice, were fixed in formalin for 24 hours, dehydrated, and embedded in paraffin. Sections of 6 μm thickness were prepared, dried, dewaxed with xylene, rehydrated through graded alcohols, and stained with hematoxylin (Servicebio, cat#G1004, CN) and eosin (Beyotime, cat#C0109, CN). Following dehydration and mounting with neutral resin, slides were scanned for H&E assessment.

Masson's trichrome staining (Solarbio, cat#G1346, CN) was performed on mouse back skin sections according to the manufacturer's instructions, using the same section preparation procedure. Toluidine blue staining (Servicebio, cat#G2543, CN) was applied to CIA mouse knee joint sections, while Safranin O/Fast Green staining (Sigma-Aldrich, cat#F7258-25G, USA) (MCE, Cat#HY-D0215, USA) was performed on CIA ankle joint sections to evaluate cartilage integrity.

IHC staining

For the spleen sections of the IMQ mouse model, after rehydration, they were blocked with 10% goat serum (Beyotime, CN) and incubated overnight at 4 °C with IL-17A monoclonal antibody (Invitrogen, cat#14-7179-82, USA). For the knee joint sections of the CIA model, they were incubated with IL-17A, RORγt (Abcam, cat#ab207082, USA), TNF (Abcam, cat#ab307164, USA), IL-6 (Abcam, cat#ab290735, USA), and MMP3 (Abcam, cat#ab52915, USA) monoclonal antibody. The next day, sections were treated with a goat anti-rabbit secondary antibody (Abcam, cat#ab6721, USA) or goat anti-mouse secondary antibody (Abcam, cat#ab6789, USA) for 1 hour, developed with DAB (Abcam, cat#ab64238, USA), mounted, and scanned for IHC results.

IF staining

Affected skin of the IMQ mouse model and spleen from the CIA mouse model were flash-frozen, embedded in OCT, and cryo-sectioned at 6 μm. After warming to room temperature, sections were fixed with 4% paraformaldehyde, blocked with 10% goat serum, and incubated overnight at 4 °C with IL-17A monoclonal antibody, Anti-ROR gamma, or CD4 monoclonal antibody. In addition, frozen skin sections were also stained with IL-21 monoclonal antibody (eBioscience, cat#16-7211-82, USA) and IL-22 monoclonal antibody (eBioscience, cat#16-7222-82, USA). The next day, they were treated with Goat Anti-Mouse IgG H&L (Alexa Fluor® 647) (Abcam, cat#ab150225, USA) or Goat Anti-Rabbit IgG H&L (Alexa Fluor® 488) (Abcam, cat#ab150077, USA). Finally, sections were mounted using a DAPI medium and imaged with a confocal microscope (ZEISS, SUPRA55#, Germany).

Flow cytometry analysis of Th17 cells in the spleen of CIA mice

Fresh spleens were harvested from CIA model mice in each experimental group. The tissues were mechanically dissociated using a mesh filter, passed through a 100 μm cell strainer, subjected to red blood cell lysis, and resuspended in PBS for cell counting. To block Fc receptor binding, 1×10^6 cells were pre-incubated with Ms CD16/CD32 Pure 2.4G2 (BD, cat# BD553141, USA). Surface staining for CD4 was performed using FITC-conjugated anti-CD4 monoclonal antibody. Subsequently, cells were fixed and permeabilized using the Cytofix/Cytoperm Soln Kit (BD, cat# BD554714, USA) before intracellular staining with Alexa 647-conjugated anti-IL-17A monoclonal antibody (BD, cat# BD560184, USA). Following staining and washing, cells were analyzed via flow cytometry to quantify the proportion of Th17 ($CD4^+IL\text{-}17A^+$) cells in the spleen. All antibodies used for IHC and IF staining, including their detailed information and working concentrations, are listed in Supplementary Table 1.

Statistical & reproducibility

Data are expressed as mean ± SD, with sample sizes detailed in the figure legends. Differences between groups were evaluated using unpaired Student's t-tests or one-way/two-way ANOVA, followed by Tukey's post hoc tests, as specified. In vivo experiments involved 5 to 10 mice per condition. A p-value of ≤ 0.05 was considered statistically significant, and values less than 0.0001 are reported as $p < 0.0001$. All statistical analyses were performed using GraphPad Prism 8 software.

Ethic statement

All animal handling and use was approved by the Institutional Animal Care and Use Committee (IACUC) of Shenzhen Institutes of Advanced Technology, Chinese Academy of Sciences. The study involving CIA mice was approved under registration number SIAT-IACUC-210901-YGS-WY-A2044 on September 17, 2021, and the study involving IMQ-induced mice was approved under registration number SIAT-IACUC-240409-YGS-WY-A2588 on April 18, 2024. All procedures were conducted in accordance with the ARRIVE guidelines for reporting animal research. All mice used in the study were male to ensure model consistency and minimize variability; sex was not considered a biological variable, as CIA is more susceptible in males, and IMQ-induced PO inflammation does not show strong sex bias.

Reporting summary

Further information on research design is available in the Nature Portfolio Reporting Summary linked to this article.

Data availability

The RNA-seq raw data have been deposited in the Genome Sequence Archive in the National Genomics Data Center, China National Center for Bioinformation / Beijing Institute of Genomics, Chinese Academy of Sciences, under the accession code CRA031231. All data are included in the Supplementary Information or available from the authors, as are unique reagents used in this Article. The raw numbers for charts and graphs are available in the Source Data file whenever possible. Source data are provided with this paper.

References

1. Cheng, L. et al. Human umbilical cord mesenchymal stem cells for psoriasis: a phase 1/2a, single-arm study. *Signal Transduct. Target Ther.* **7**, 263 (2022).
2. Chen, H. et al. Treatment of Psoriasis with Mesenchymal Stem Cells. *Am. J. Med.* **129**, e13–e14 (2016).
3. Yao, D. et al. Adipose-derived mesenchymal stem cells (AD-MSCs) in the treatment for psoriasis: results of a single-arm pilot trial. *Ann. Transl. Med.* **9**, 1653 (2021).
4. Sun, L. et al. Mesenchymal stem cell transplantation reverses multiorgan dysfunction in systemic lupus erythematosus mice and humans. *Stem Cells* **27**, 1421–1432 (2009).

5. Liang, J. et al. Allogenic mesenchymal stem cells transplantation in refractory systemic lupus erythematosus: a pilot clinical study. *Ann. Rheum. Dis.* **69**, 1423–1429 (2010).
6. Cao, Z. et al. Allogenic Umbilical Cord-Derived Mesenchymal Stromal Cells Sustain Long-Term Therapeutic Efficacy Compared With Low-Dose Interleukin-2 in Systemic Lupus Erythematosus. *Stem Cells Transl. Med.* **12**, 431–443 (2023).
7. Alanazi, A., Alassiri, M., Jawdat, D. & Almalik, Y. Mesenchymal stem cell therapy: A review of clinical trials for multiple sclerosis. *Regen. Ther.* **21**, 201–209 (2022).
8. Forbes, G. M. et al. A phase 2 study of allogeneic mesenchymal stromal cells for luminal Crohn's disease refractory to biologic therapy. *Clin. Gastroenterol. Hepatol.* **12**, 64–71 (2014).
9. Lightner, A. L. et al. A phase IB/IIA study of remestemcel-L, an allogeneic bone marrow-derived mesenchymal stem cell product, for the treatment of medically refractory ulcerative colitis: an interim analysis. *Colorectal Dis.* **24**, 1358–1370 (2022).
10. Gregoire, C. et al. Review article: mesenchymal stromal cell therapy for inflammatory bowel diseases. *Aliment Pharm. Ther.* **45**, 205–221 (2017).
11. Hwang, J. J., Rim, Y. A., Nam, Y. & Ju, J. H. Recent Developments in Clinical Applications of Mesenchymal Stem Cells in the Treatment of Rheumatoid Arthritis and Osteoarthritis. *Front. Immunol.* **12**, 631291 (2021).
12. Ghoryani, M. et al. Amelioration of clinical symptoms of patients with refractory rheumatoid arthritis following treatment with autologous bone marrow-derived mesenchymal stem cells: A successful clinical trial in Iran. *Biomed. Pharmacother.* **109**, 1834–1840 (2019).
13. Li, C. et al. Mesenchymal Stem Cells-Involved Strategies for Rheumatoid Arthritis Therapy. *Adv. Sci.* **11**, e2305116 (2024).
14. Corcione, A. et al. Human mesenchymal stem cells modulate B-cell functions. *Blood* **107**, 367–372 (2006).
15. Shen, Z. W. et al. Effects of mesenchymal stem cell-derived exosomes on autoimmune diseases. *Front. Immunol.* **12**, https://doi.org/10.3389/fimmu.2021.749192 (2021).
16. Song, N., Scholtemeijer, M. & Shah, K. Mesenchymal Stem Cell Immunomodulation: Mechanisms and Therapeutic Potential. *Trends Pharm. Sci.* **41**, 653–664 (2020).
17. Ra, J. C. et al. Stem cell treatment for patients with autoimmune disease by systemic infusion of culture-expanded autologous adipose tissue derived mesenchymal stem cells. *J. Transl. Med.* **9** https://doi.org/10.1186/1479-5876-9-181 (2011).
18. Hong, H. S., Kim, Y. H. & Son, Y. Perspectives on mesenchymal stem cells: tissue repair, immune modulation, and tumor homing. *Arch. Pharmacal Res.* **35**, 201–211 (2012).
19. El-Badri, N. S., Maheshwari, A. & Sanberg, P. R. Mesenchymal stem cells in autoimmune disease. *Stem Cells Dev.* **13**, 463–472 (2004).
20. Berglund, A. K., Fortier, L. A., Antczak, D. F. & Schnabel, L. V. Immunoprivileged no more: measuring the immunogenicity of allogeneic adult mesenchymal stem cells. *Stem Cell Res. Ther.* **8** https://doi.org/10.1186/s13287-017-0742-8 (2017).
21. Squillaro, T., Peluso, G. & Galderisi, U. Clinical trials with mesenchymal stem cells: an update. *Cell Transplant.* **25**, 829–848 (2016).
22. Blázquez-Prunera, A., Díez, J. M., Gajardo, R. & Grancha, S. Human mesenchymal stem cells maintain their phenotype, multipotentiality, and genetic stability when cultured using a defined xeno-free human plasma fraction. *Stem Cell Res Ther.* **8**, 103 (2017).
23. Sarkar, D. et al. Engineered cell homing. *Blood* **118**, E184–E191 (2011).
24. Huang, X. L. et al. Design considerations of iron-based nanoclusters for noninvasive tracking of mesenchymal stem cell homing. *Acs Nano* **8**, 4403–4414 (2014).
25. Ullah, M., Liu, D. D. & Thakor, A. S. Mesenchymal stromal cell homing: mechanisms and strategies for improvement. *iScience* **15**, 421–438 (2019).
26. Cuesta-Gomez, N., Graham, G. J. & Campbell, J. D. M. Chemokines and their receptors: predictors of the therapeutic potential of mesenchymal stromal cells. *J. Transl. Med.* **19**, 156 (2021).
27. Galipeau, J. & Sensébé, L. Mesenchymal stromal cells: clinical challenges and therapeutic opportunities. *Cell Stem Cell* **22**, 824–833 (2018).
28. Dhoke, N. R., Kaushik, K. & Das, A. Cxcr6-based mesenchymal stem cell gene therapy potentiates skin regeneration in murine diabetic wounds. *Mol. Ther.* **28**, 1314–1326 (2020).
29. Kuang, S. H. et al. CCR2-engineered mesenchymal stromal cells accelerate diabetic wound healing by restoring immunological homeostasis. *Biomaterials* **275** https://doi.org/10.1016/j.biomaterials.2021.120963 (2021).
30. Wei, W., Huang, Y., Li, D., Gou, H. F. & Wang, W. Improved therapeutic potential of MSCs by genetic modification. *Gene Ther.* **25**, 538–547 (2018).
31. Kovtun, Y. V. & Goldmacher, V. S. Cell killing by antibody-drug conjugates. *Cancer Lett.* **255**, 232–240 (2007).
32. Tolcher, A. W. Antibody drug conjugates: lessons from 20 years of clinical experience. *Ann. Oncol.* **27**, 2168–2172 (2016).
33. Fu, Z. W., Li, S. J., Han, S. F., Shi, C. & Zhang, Y. Antibody drug conjugate: the "biological missile" for targeted cancer therapy. *Signal Transduct. Target. Ther.* **7** https://doi.org/10.1038/s41392-022-00947-7 (2022).
34. Raphael, I., Joern, R. R. & Forsthuber, T. G. Memory CD4$^+$ T Cells in immunity and autoimmune diseases. *Cells* **9** https://doi.org/10.3390/cells9030531 (2020).
35. Yan, J. W. et al. Therapeutic potential of interleukin-17 in inflammation and autoimmune diseases. *Expert Opin. Ther. Tar.* **18**, 29–41 (2014).
36. Wilson, N. J. et al. Development, cytokine profile and function of human interleukin 17-producing helper T cells. *Nat. Immunol.* **8**, 950–957 (2007).
37. Iwakura, Y. & Ishigame, H. The IL-23/IL-17 axis in inflammation. *J. Clin. Investig.* **116**, 1218–1222 (2006).
38. Hu, H., Li, H., Li, R., Liu, P. & Liu, H. Re-establishing immune tolerance in multiple sclerosis: focusing on novel mechanisms of mesenchymal stem cell regulation of Th17/Treg balance. *J. Transl. Med.* **22**, 663 (2024).
39. Manel, N., Unutmaz, D. & Littman, D. R. The differentiation of human TH-17 cells requires transforming growth factor-β and induction of the nuclear receptor RORγt. *Nat. Immunol.* **9**, 641–649 (2008).
40. Ma, S. Y. et al. RORγt phosphorylation protects against T cell-mediated inflammation. *Cell Rep.* **38** https://doi.org/10.1016/j.celrep.2022.110520 (2022).
41. Maier, C. S. et al. Cedirogant Population Pharmacokinetics and Pharmacodynamic Analyses of Interleukin-17A Inhibition in Two Phase 1 Studies in Healthy Participants and Participants with Moderate to Severe Psoriasis. *Clin. Pharm. Drug Dev.* **13**, 474–484 (2024).
42. Sun, N. N., Guo, H. M. & Wang, Y. H. Retinoic acid receptor-related orphan receptor gamma-t (RORγt) inhibitors in clinical development for the treatment of autoimmune diseases: a patent review (2016-present). *Expert Opin. Ther. Pat.* **29**, 663–674 (2019).
43. Chen, Z. et al. Engineered enucleated mesenchymal stem cells regulating immune microenvironment and promoting wound healing. *Adv. Mater.* **36**, e2412253 (2024).
44. Wratil, P. R., Horstkorte, R. & Reutter, W. Metabolic Glycoengineering with N-Acyl Side Chain Modified Mannosamines. *Angew. Chem. Int Ed. Engl.* **55**, 9482–9512 (2016).
45. Beccari, M. V. et al. Ibalizumab, a novel monoclonal antibody for the management of multidrug- resistant HIV-1 infection. *Antimicrob. Agents Chemother.* **63** https://doi.org/10.1128/aac.00110-19 (2019).
46. Gege, C. Retinoic acid-related orphan receptor gamma t (RORγt) inverse agonists/antagonists for the treatment of inflammatory

diseases - where are we presently? *Expert Opin. Drug Discov.* **16**, 1517–1535 (2021).
47. Tyring, S. et al. Cedirogant in adults with psoriasis: a phase II, randomized, placebo-controlled clinical trial. *Clin. Exp. Dermatol.* **49**, 1347–1355 (2024).
48. Weinreb, M. et al. Prostaglandin E2 (PGE2) increases the number of rat bone marrow osteogenic stromal cells (BMSC) via binding the EP4 receptor, activating sphingosine kinase and inhibiting caspase activity. *Prostaglandins Leukotrienes Essent. Fat. Acids* **75**, 81–90 (2006).
49. Jiang, N. Z. et al. Fibroblast growth factor 2 enhances BMSC stemness through ITGA2-dependent PI3K/AKT pathway activation. *J. Cell. Physiol.* **239** https://doi.org/10.1002/jcp.31423 (2024).
50. Jia, H. Y. et al. Lenalidomide attenuates IMQ-induced inflammation in a mouse model of psoriasis. *Biomed. Pharmacother.* **156**, https://doi.org/10.1016/j.biopha.2022.113883 (2022).
51. González, M. A., Gonzalez-Rey, E., Rico, L., Büscher, D. & Delgado, M. Treatment of experimental arthritis by inducing immune tolerance with human adipose-derived mesenchymal stem cells. *Arthritis Rheum.* **60**, 1006–1019 (2009).
52. Xie, X. -j. et al. Indirubin ameliorates imiquimod-induced psoriasis-like skin lesions in mice by inhibiting inflammatory responses mediated by IL-17A-producing γδ T cells. *Mol. Immunol.* **101**, 386–395 (2018).
53. Brand, D. D., Latham, K. A. & Rosloniec, E. F. Collagen-induced arthritis. *Nat. Protoc.* **2**, 1269–1275 (2007).
54. Griffiths, C. E. M., Armstrong, A. W., Gudjonsson, J. E. & Barker, J. N. W. N. Psoriasis. *Lancet* **397**, 1301–1315 (2021).
55. Smolen, J. S., Aletaha, D. & McInnes, I. B. Rheumatoid arthritis. *Lancet* **388**, 2023–2038 (2016).
56. Lerner, A., Neidhöfer, S., Reuter, S. & Matthias, T. MMP3 is a reliable marker for disease activity, radiological monitoring, disease outcome predictability, and therapeutic response in rheumatoid arthritis. *Best. Pract. Res. Clin. Rheumatol.* **32**, 550–562 (2018).
57. Reich, K. et al. Bimekizumab versus Secukinumab in Plaque Psoriasis. *N. Engl. J. Med* **385**, 142–152 (2021).
58. Wang, Y. H. et al. From RORγt Agonist to Two Types of RORγt Inverse Agonists. *ACS Med. Chem. Lett.* **9**, 120–124 (2018).
59. Huang, P. X., Chandra, V. & Rastinejad, F. Structural overview of the nuclear receptor superfamily: insights into physiology and therapeutics. *Annu. Rev. Physiol.* **72**, 247–272 (2010).
60. Ohara, D., Takeuchi, Y. & Hirota, K. Type 17 immunity: novel insights into intestinal homeostasis and autoimmune pathogenesis driven by gut-primed T cells. *Cell. Mol. Immunol.* **21**, 1183–1200 (2024).
61. Tahir, H. et al. Secukinumab in Active rheumatoid arthritis after anti-TNFα therapy: a randomized, double-blind placebo-controlled Phase 3 Study. *Rheumatol. Ther.* **4**, 475–488 (2017).
62. Murata, M. & Teshima, T. Treatment of steroid-refractory acute graft-versus-host disease using commercial mesenchymal stem cell products. *Front. Immunol.* **12** https://doi.org/10.3389/fimmu.2021.724380 (2021).
63. Liang, J. H. et al. Incidence of collagen-induced arthritis is elevated by a high-fat diet without influencing body weight in mice. *RMD Open* **10** https://doi.org/10.1136/rmdopen-2023-003869 (2024).

Acknowledgements

This work was supported by National Key R&D Program of China (2024YFF1206400, 2023YFA1801500), National Natural Science Foundation of China (82174033, 32270830, T2350710233), the Nature Science Foundation of Jiangsu Province (BK20230026), Southeast University Interdisciplinary Research Program for Young Scholars (2024FGC1003), Shenzhen Science and Technology Key Program (JCYJ20220818101404009), and Guangdong Provincial Key Laboratory of Multimodality Non-Invasive Brain-Computer Interfaces (2024B1212010010).

Author contributions

Conceptualization, Q.X., and Y.W., Methodology, Q.X., Y.N.S., J.H.L., S.Y.H., and C.F., Investigation, X.F.D., Y.W., Validation and Data Curation, Q.X., and Y.N.S., Resources, B.S., Writing – Original Draft, Q.X., Y.N.S., and Y.W.; Writing – Review & Editing, Q.X. and Y.W.; Supervision, Y.W.; Funding Acquisition, B.S., L.C., and Y.W.

Competing interests

The authors declare the following competing interests: Q.X., Y.N.S., J.H.L., and Y.W. are named as inventors on a granted patent (ZL202411354633.2) filed by Shenzhen Institutes of Advanced Technology, which relates to the technology described in this manuscript. The remaining authors declare no competing interests.

Additional information

Supplementary information The online version contains supplementary material available at https://doi.org/10.1038/s41467-025-67698-1.

Correspondence and requests for materials should be addressed to Qian Xie, Lei Chen or Yan Wang.

Peer review information *Nature Communications* thanks Sujata Mohanty, who co-reviewed with Yashvi Sharma and Antonio Uccelli, who co-reviewed with Giada Pessina, for their contribution to the peer review of this work. A peer review file is available.